MODELS AND ALGORITHMS FOR SPECTRUM COEXISTENCE IN WIRELESS NETWORKS

BY SHWETA S. SAGARI

A dissertation submitted to the

Graduate School—New Brunswick

Rutgers, The State University of New Jersey

in partial fulfillment of the requirements

for the degree of

Doctor of Philosophy

Graduate Program in Electrical and Computer Engineering

Written under the direction of

Dr. Wade Trappe

Dr. Dipankar Raychaudhuri

Dr. Larry Greenstein

and approved by

_____

_____

_____

_____

New Brunswick, New Jersey

May, 2016

© 2016

Shweta S. Sagari

ALL RIGHTS RESERVED

ABSTRACT OF THE DISSERTATION

Models and Algorithms for Spectrum Coexistence in Wireless Networks

by Shweta S. Sagari

Dissertation Director: Dr. Wade Trappe

Dr. Dipankar Raychaudhuri

Dr. Larry Greenstein

In the last decade, there have been several technological trends that have occurred together and have caused a shift in how wireless systems will be deployed. The significant increase in the capabilities of mobile devices, combined with the proliferation of Internet enabled services, and the improvement in the communication support provided by new waveforms for wireless communications, have initiated a shift from the traditional, macrocell-based cellular network to new forms of radio access technologies (RATs) involving multiple, smaller cells deployed in vicinity of each other. These small cells will often support diverse wireless technologies and be operated by different providers. The resulting heterogeneity, unfortunately, can lead to serious internetwork interference that can negate the improvement in overall system performance that was the original motivation for employing many small cells in close proximity. In this thesis, we examine different technologies that are needed for flexible spectrum management to support the coordination that is needed for coexistence between many small cell wireless networks. Motivated by the need for internetwork architectures that support spectrum coordination, we (1) conduct performance evaluation associated with the joint

deployment of mobile and fixed hotspot networks, (2) develop spectrum models that characterize interference among different wireless entities, (3) provide new methods for efficient hardware emulation of wireless channels, (4) devise algorithms that estimate radio spectrum usage, and (5) provide algorithms for coordination between different wireless systems to improve the overall system performance and spectrum efficiency.

The first part of the thesis investigates spectrum coexistence in wireless networks by exploring the underlying performance challenges that exist when mobile hotspots are deployed in an environment of densely deployed, static wireless access networks. Next part of thesis investigates design of hardware emulator of radio channels to accurately capture the effect of real-world wireless channels upon communications waveforms while minimizing computational complexity. Next, we explore a fundamental building block of spectrum management for supporting better utilization of radio spectrum which involves predicting the impact that an emitter will have at different geographic locations. We then examine various challenges associated with coordinating spectrum access between different wireless technologies by exploring the specific case of Wi-Fi and LTE coexistence in emerging unlicensed frequency bands.

Finally, recognizing the broad challenges associated with addressing spectrum coexistence in emerging wireless systems, we identify several directions for future investigation and suggest different approaches for tackling these challenges.

Acknowledgements

"Life is a journey, not a destination."

– Ralph Waldo Emerson

My graduate school journey over the last six years could not have been described more aptly than this favorite quote of mine. When I landed in the US for my master's, my plan was to do master's and take a job. But then WINLAB happened which changed me fundamentally in the way I function and think, for which I always be grateful. I feel fortunate to be guided by Prof. Wade Trappe, Prof. Dipankar Raychaudhuri and Dr. Larry Greenstein, whose working style though differ from each other, made my experience a wholesome with their technical and life advice and constant support. Prof. Ray has always inspired me with his simplicity of logic, heuristic approach and acute engineering insights. Wade drove my thought process to new ideas that I can immediately connect with. I never failed to be amazed how Larry's casual technical intuitions are always close to the profound theory.

I would also like to thank Prof. Narayan Mandayam, Prof. Roy Yates for being on my proposal committee and Dr. Milind Buddhikot for being on my thesis committee, and for their advice and suggestions regarding the thesis. Prof. Yates's urge to dive into basics of a problem and Prof. Mandayam's attention to details have helped me building understanding of systems during coursework and summer internship at WINLAB.

I have learnt a lot through discussions with Ivan Seskar whose encyclopedia knowledge of systems and networking, passion and practical insights into the problem always inspires me. During the course of the thesis, I am also grateful to my collaborators in WINLAB including Dr. Gautam Bhanage, Dr. Akash Baid, Dr. Dola Saha, and Dr. Krishna Balchandran, Dr. Kiran Rege, Dr. Joseph Kang, Dr. Kemal Karakayali at Bell Labs, and Dr. Prabhakar Chitrapu at InterDigital who have helped me shape my

research work. Furthermore, graduate assistantship support from the National Science Foundation, grants FIA NP CNS-134529 (2014-current),FIA CNS-1040735 (2010-14), SAVANT CNS- 1247764 are gratefully acknowledged. I would like to thank the staff at WINLAB, Department of Electrical and Computer Engineering, and International Student Office for their excellent academic and technical support.

I would like to acknowledge all group mates, WINLAB colleagues and friends who have been my family away from home and supported me in my good/bad times. I refrain from mentioning individual names lest I forget someone - but life in Rutgers would not be enjoyable without you guys. Finally, I would like to thank my family - my father Suresh Sagari and mother Pushpalata Sagari who have always supported me out of their way and many times their social beliefs to make my dreams, may it be small, into the reality, my sister Gauri who has always been my guide, friend and care-taker from the childhood, my father-in-law Hiraman Supekar for being tenacious and mother-in-law Anjali Supekar for her evergreen enthusiasm and positivity. Last but not least, I would like to thank my husband Abhijit who has made last three years much easier for me with his understanding and support. I would have struggled to complete my thesis without him by my side.

Dedication

To Aji (Grandma), Aai (Mom), Baba (Dad), Didi (Sister), and a few special people in my life. This thesis is a dedication to all of them.

Table of Contents

Abstract ii

Acknowledgements iv

Dedication vi

List of Tables xi

List of Figures xii

1. Introduction 1

1.1. The need for Spectrum Management 1

1.2. Dynamic Spectrum Management 3

1.2.1. Focus of Thesis: Modeling and Algorithm Framework 3

1.2.2. Network Architecture: Enabler for the Proposed Framework . . . 5

1.3. Thesis Organization 6

2. Performance Evaluation of Mobile Wi-Fi Hotspots in Densely Deployed Fixed Wi-Fi Networks 8

2.1. Modeling Coexistence of Fixed and Mobile Wi-Fi APs 10

2.1.1. Deployment Scenario 10

2.1.2. Heterogeneity in Network 11

2.1.3. Performance at Mobile Wi-Fi AP 13

2.2. Adaptive Channel Assignment 13

2.2.1. Increase in Throughput at Mobile Wi-Fi AP 14

2.2.2. Effect of Density of Fixed W-Fi APs 15

2.3. Adaptive Channel Assignment with High Mobility 16

3. Emulating Multipath Channel in Wireless Network using Equivalent Reduced Taps 19

3.1. Emulating Direct Communication Link using Equivalent Reduced-Tap Filters 21

3.1.1. Approach 21

3-tap Channel Approximation 21

3.1.2. The Exponential Channel 23

Generic Channel Impulse Response 23

The Exponential Power Delay Profile 24

3.1.3. Channel with Reduced Taps 25

A Moment-matching 3-tap Channel Approximation 25

An Ad-hoc 3-tap Channel Approximation 26

3.1.4. Evaluation 26

Evaluation Methodology 26

Results 28

3.2. Emulating Co-Channel Interference Using Equivalent Reduced-Tap Filters 31

3.2.1. Approach 32

3.2.2. The Exponential Interference Channel 32

Total Instantaneous Interference Power 33

Analysis of the Exponential PDP 35

3.2.3. Emulator Channel with Reduced Taps 37

The n-tap Channel Approximation 37

Analysis of the n-tap PDP 38

Required Number of Taps Per Link, n 39

3.2.4. Results 40

The n-tap Channel Approximation 40

An Alternative Approach for $Mn \geq 16$ 41

4. Practical Interpolation for Spectrum Cartography through Local Path Loss Modeling . . . 43

4.1. Radio Mapping Approach . . . 43

4.2. The Stochastic Method . . . 44

4.2.1. Spatial Correlation of Shadow Fading . . . 45

4.2.2. The Ideal Case: SM-0 . . . 45

4.2.3. Determining μ_0 and σ_0 . . . 46

4.3. Reducing the Stochastic Method to Practice . . . 48

4.3.1. The First Method, SM-1 . . . 48

4.3.2. The Second Method: SM-2 . . . 51

4.4. Evaluation . . . 51

4.4.1. Methodology . . . 51

4.4.2. Effect of Sensor Spacing . . . 54

4.4.3. Effect of Emitter Location . . . 56

4.4.4. Effect of Correlation Function . . . 56

Gaussian correlation function . . . 56

Elliptical correlation function . . . 56

4.5. Discussion . . . 57

5. Coordinated Dynamic Spectrum Management of LTE and Wi-Fi Networks . . . 60

5.1. Background on Wi-Fi/LTE Co-existence . . . 60

5.2. Interference Characterization . . . 63

5.2.1. Interference Characterization Model . . . 63

Characterization of Wi-Fi Throughput . . . 64

Characterization of LTE Throughput . . . 65

5.2.2. Experimental Validation . . . 66

5.2.3. Motivational Example . . . 69

5.3. System Model . . . 71

5.4. Coordination via Joint Optimization 74
5.4.1. Joint Power Control Optimization 74
5.4.2. Joint Time Division Channel Access Optimization 76
Power control optimization across network of same RAT 77
Joint time division channel access optimization 77
5.5. Evaluation of Joint Coordination 78
5.5.1. Single Link Co-channel Deployment 78
5.5.2. Multiple Links Co-channel Deployment 79

6. Conclusion 84

References 87

List of Tables

2.1. Simulation parameters of Fixed and Mobile AP 11

3.1. Some Notations and Definitions 23

3.2. Discrepancies (dB) in SNR at $<BER>= 10^{-8}$ 31

3.3. Some Notations and Definitions 33

3.4. Number of taps n as a function of $W\tau_{rms}$ 39

4.1. Notation description 47

4.2. Simulation parameters 53

5.1. Network parameters of Wi-Fi/LTE deployment 69

5.2. Definition of notations 73

List of Figures

1.1. Proposed spectrum bands for deployment of wireless small cells. 2

1.2. Typical heterogeneous network with multiple RATs and owned by multiple operators 3

1.3. Enabler architecture for inter-network cooperation on radio resource management (prior work at WINLAB) 6

1.4. Thesis components 7

2.1. Co-existing scenario of fixed and mobile APs 9

2.2. Throughput at a mobile AP as a function of number of fixed APs in the carrier sense of the mobile AP. 13

2.3. Random deployment of Fixed APs and the trajectory of the mobile AP. 14

2.4. Optional caption for list of figures 15

2.5. Optional caption for list of figures 16

2.6. Throughput at mobile AP (Mbps) when ACA is applied, as a function of ACA scanning period (sec) for a fixed density of 50 APs/km^2 18

3.1. Network with $N = 6$ nodes, and three simultaneous communications links. Node D is receiving a desired signal from Node A and $M = 2$ interferers, from Nodes C and E. 20

3.2. CDFs of the Noise Peaking Factor (NPF) comparing with 3-tap moment-matching channel 29

3.3. *BER* vs. *SNR* for 4-QAM Signaling comparing with 3-tap moment-matching channel 30

3.4. Quantile-quantile plots of z for an exponential PDP with $W\tau_{rms} = 16$ and $M = 2, 4, 6$. For each M, the plot shows the closeness of z to a Gaussian variable of the same mean and variance (red dashed line). . . . 34

3.5. Number of taps n per link: Comparison of $n = \coth(1/(2W\tau_{rms}))$ from analysis $n =(\mathrm{Max}(1, 2 * W\tau_{rms}))$ 40
3.6. CDFs of z for n-tap channel and true (exponential) channel, when the number of interfering links is $M = 2, 4, 6$ and $n = 2W\tau_{rms}$. 41
3.7. CDFs of z for n-tap channel approximation with $n = 8$ in comparison with an exponential PDP with $W\tau_{rms} = 16$ for interfering links $M = 2$. 42
4.1. Problem geometry to be studied. The sensor layout defines a square grid, with each square having side D. Computations are made for the square shown shaded, with sensors 1, 2, 3 and 4. Interpolation methods are applied to points inside the square to estimate received power from the emitter at location E. 52
4.2. Optional caption for list of figures 53
4.3. Optional caption for list of figures 54
4.4. Optional caption for list of figures 55
4.5. Optional caption for list of figures 57
5.1. Scenarios showing challenges of LTE and Wi-Fi coexistence in the same unlicensed spectrum. 61
5.2. Experimental scenario to evaluate the throughput performance of Wi-Fi w_1 in the presence of interference (LTE/other Wi-Fi/white noise) when both w_1 and interference operated on the same channel in 2.4 GHz . . . 67
5.3. Comparative results analytical model and experiments to show the effect of LTE on the throughput of Wi-Fi 802.11g when distance between LTE eNB and Wi-Fi link is varied. 67
5.4. Comparative results analytical model and experiments to show the effect of LTE on the throughput of Wi-Fi 802.11g when distance between LTE HeNB (AP) and Wi-Fi link is varied. 68
5.5. Experimental scenario to evaluate the throughput performance of Wi-Fi w_1 in the presence of interference (LTE/other Wi-Fi/white noise) when both w_1 and interference operated on the same channel in 2.4 GHz . . . 70

5.6. Optional caption for list of figures 71
5.7. Optional caption for list of figures 72
5.8. Optional caption for list of figures 81
5.9. Optional caption for list of figures 82
5.10. 10 percentile and mean LTE throughput for a single link Wi-Fi and LTE co-channel deployment 83
5.11. Optional caption for list of figures 83

Chapter 1

Introduction

Exponential growth in mobile data usage is driven multitude of Internet applications that are rapidly migrating from wired PCs to mobile smartphones, tablets, phablets, mobile APs, wearable and Internet-of-Things (IoT) devices [1–4]. The number of global mobile devices is expected to grow from 8 billions today to 20 billion by the year 2020 [5]. According to Cisco's 2015 VNI report, compound annual growth rate (CAGR) of data traffic is projected to grow 53 % from year 2015 to 2020, especially with the increase mobile video traffic.

This growth of mobile traffic requires mobile devices with various long- and short-distance wireless technologies to coexist in time, frequency, and spatial domains. Thus, there is urgent need to study spectrum access techniques that maximize area spectrum efficiency (measured in bps/Hz/sq-Km) independent of number of devices in the network. This thesis, therefore, investigates dynamic spectrum management to tackle such ever increasing data demand. The salient outcome of this thesis are new wireless tools which allow to (1) measure spectrum usage, (2) characterize interference among wireless technologies and (3) propose coordination algorithm.

1.1 The need for Spectrum Management

Recent PCAST report advocates increase of reliance on shared spectrum using dynamic and flexible management system with more granular control on available resources [6,7]. The spectrum could be shared under licensed, unlicensed, or new sharing models. Several spectrum bands, as shown in figure 1.1, like TV white space, 3.5 GHz, mmWave,

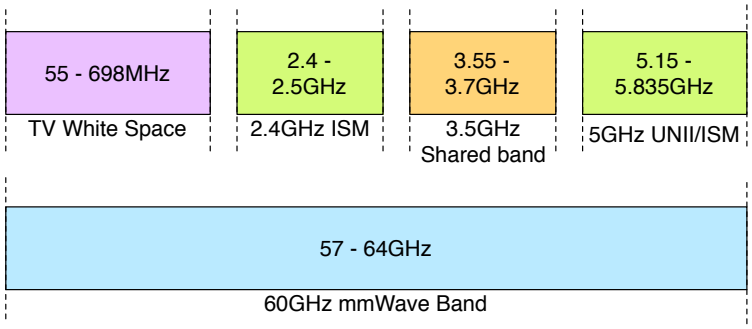

Figure 1.1: Proposed spectrum bands for deployment of wireless small cells.

unlicensed 2.4/5 GHz bands have been opened up for mobile and fixed wireless broadband services [8–12]. These emerging shared band scenarios will lead to co-channel network deployment of multiple radio access technologies (RATs) by multiple operators. These coexisting networks cause increased interference to each other and degradation of the overall system performance, if no coordination is provided.

Conventionally, spectrum usage has been limited to scheduler like resource (time / frequency) assignment for licensed spectrum or reactive spectrum sensing protocols like Listen-Before-Talk (LBT) for unlicensed spectrum. These protocols have limited local network visibility and does not coordinate networks that belong to different RATs and/or operator [13–15]. In previous work, next level of network operation is proposed by schemes like regional statistical spectrum multiplexing through 'spectrum broker' [16, 17], spectrum server [18], radio-based common control channels [17, 19] to distribute operating parameters of co-existing radio networks. Most recently, database driven centralized 'spectrum assignment server' (SAS) [20, 21] eliminates the requirement of spectrum sensing and relies on database of incumbents for dynamic spectrum coordination. The main disadvantage of such spectrum server is the failure to update database (thus, spectrum usage) on granular time scale of minutes/seconds. With billions of operating radio devices, such central database could face the network bottleneck. Thus,we need spectrum management framework which is distributed in nature in order to scale spectrum allocation with time scales of minutes/second. Furthermore, we need framework which can accommodate modular interfaces for dissemination of

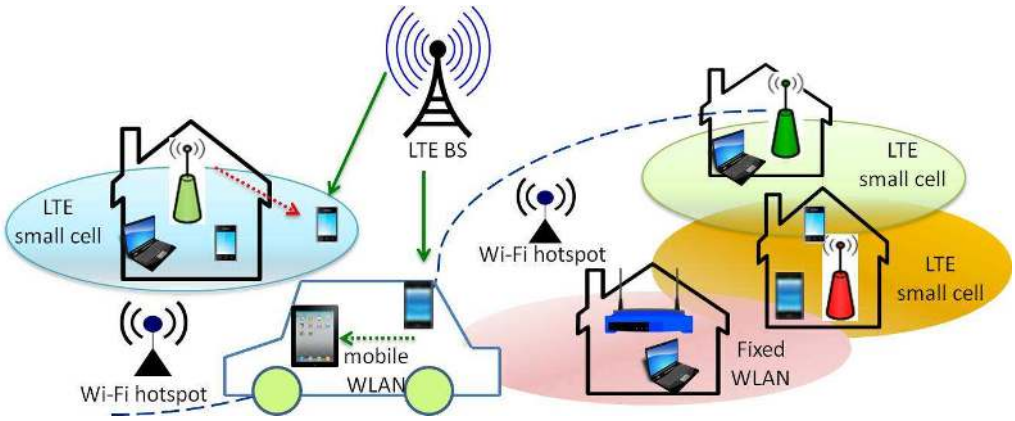

Figure 1.2: Typical heterogeneous network with multiple RATs and owned by multiple operators

spectrum usage information, interference characteristics for different spectrum bands, mobility management and algorithms. These modular interfaces make the framework technology-, operator- and spectrum band- agnostic, enable interference mitigation and improve spectrum efficiency.

1.2 Dynamic Spectrum Management

In effort to build flexible dynamic spectrum management, we need a set of standardized APIs which collect radio/spectrum information, process it, transfer the information to other APIs if necessary and set radio resource allocation parameters at wireless devices/networks. These APIs strongly rely on underlying models of coexistence characterization, spectrum usage and coordination algorithms which is the main focus of the thesis.

1.2.1 Focus of Thesis: Modeling and Algorithm Framework

This thesis focuses on co-channel operation scenarios created by coexistence of Wi-Fi and LTE small cells (see Fig. 1.2). We breakdown underlying spectrum management framework in following steps -

1. ***Modeling coexistence performance***:

   The main objective is to abstract out radio access technology (RAT) specific

MAC / PHY layer characteristics which affect its throughput when coexisting with networks belonging to same or different RAT. For this purpose, we show two scenarios - (1) coexistence of mobile WLAN with high density fixed WLANs [22] , and (2) coexistence of Wi-FI and LTE networks [12].

2. ***Performance evaluation tools for coexisting models***:

   We evaluate proposed analytical coexistence models with the help of simulations (MATLAB) and hardware experiments. We perform experimental evaluations using ORBIT testbed available at WINLAB and several open-sourced networking tools. Furthermore to support testing of wireless protocols on hardware emulator, we propose a method to emulate of multi-path wireless channel which reduces hardware computational complexity significantly for large number of coexisting nodes [23, 24].

3. ***Understanding location specific spectrum usage***:

   In this part, the objective is to build geographical region specific radio spectrum map with information such as location, frequency and perceived power levels. We propose a radio map method that uses radio measurements at sensors and exploits known properties of most path loss models, with the aim of minimizing the RMS errors in predicted dB-power. Such technique can be employed, for example, to predict the impact of radio transmission at different geographical location. This information when input in coordination algorithms leads to an efficient spectrum utilization.

4. ***Coordinated dynamic spectrum management algorithms***:

   In this study, we propose a logically centralized optimization framework that involves dynamic coordination between Wi-Fi and LTE networks by exploiting power control and time division channel access diversity. We incorporate the proposed interference characterization of Wi-Fi and LTE co-channel deployment in the optimization to account for the specific requirements of each of the technologies. Through power control optimization, aggregate throughput is maximized across all clients in both Wi-Fi and LTE networks while considering throughput

requirement for each client. Through time division channel access, we achieve the fairness among both technology based on the given policy [25].

1.2.2 Network Architecture: Enabler for the Proposed Framework

We describe an architecture for coordinating between multiple heterogeneous networks to improve spectrum utilization and facilitate co-existence which is based on the SAVANT architecture which has been proposed in earlier work at WINLAB [26] and prior architecture studies [16, 27]. Figure 1.3 shows the proposed architecture, which is built on flexible, programmable and modular architecture principles. It supports logically-centralized but geographically distributed dynamic spectrum management involving multiple autonomous networks. The basic design goal of this architecture is to support the seamless communication and information dissemination required for coordination of heterogeneous networks. This architecture leverages Internet connectivity available at most modern radio systems.

The system consists of two-tiered controllers: the Global Controller (GC) and Regional Controllers (RC), which are mainly responsible for the control plane of the architecture. The GC, owned by any neutral/authorized organization, is the main decision making entity, which acquires and processes network state information and controls the flow of information between RCs and databases based on authentication and other regulatory policies. Decisions at the GC are based on different network modules, such as radio coverage maps, coordination algorithms, policy and network evaluation matrices. The RCs are limited to network management of specific geographic regions and the GC ensures that RCs have acquired local visibility needed for radio resource allocation at wireless devices. A Local Agent (LA) is a local controller, co-located with an access point or base-station. It receives frequent spectrum usage updates from wireless clients, such as device location, frequency band, duty cycle, power level, and data rate. The signaling between RC and LAs are event-driven, which occurs in scenarios like the non-fulfillment of quality-of-service (QoS) requirements at wireless devices, request-for-update from an RC and radio access parameter updates from an RC. The key feature of this architecture is that the frequency of signaling between the different network entities

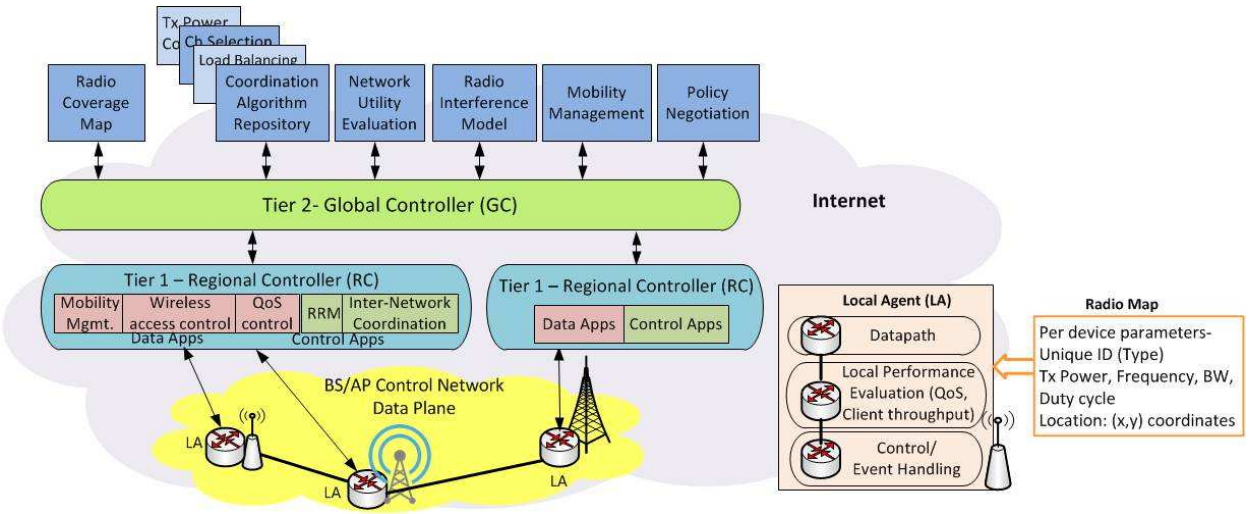

Figure 1.3: Enabler architecture for inter-network cooperation on radio resource management (prior work at WINLAB)

is less in higher tiers compared to lower tiers. RCs only control the regional messages and only wide-area network level signalling protocols are handled at the higher level, GC. Furthermore, this architecture allows adaptive network APIs like spectrum maps, mobility management, coordination algorithms, network policies and rules based on the geographic area, RAT, frequency band, Quality of Service (QoS) and traffic patterns. Thus, throughout the thesis availability of this architecture is assumed.

1.3 Thesis Organization

Overall organization of thesis is shown in Fig. 1.4. In the first part of the thesis, a dense deployment scenario for fixed and mobile WLAN is described and potential performance problems due to interference are identified. An analytical model for coexisting fixed and mobile WLAN hotspots with heterogeneous traffic is presented. An adaptive channel assignment scheme is evaluated along with the consideration of mobility speed. We then outline methods to emulate multi-node wireless network of multipath channel with the reduced computational complexity of emulation. Separate methods are proposed for emulation of direct communication link and interference links while maintaining important characteristics of channels - power delay profile and CDF of total interference

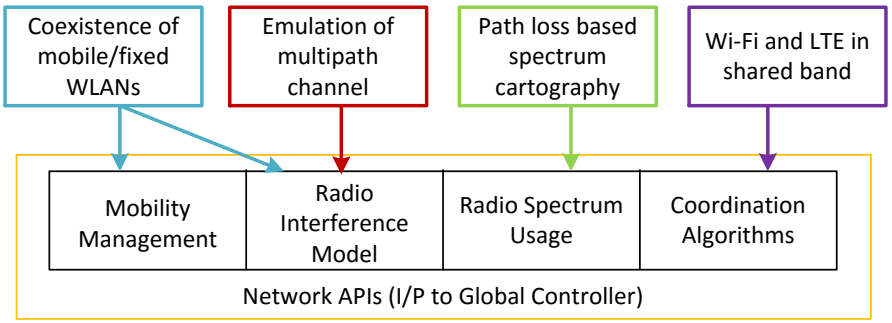

Figure 1.4: Thesis components

power, respectively.

In the next part of thesis, we examine the problem of constructing a radio map that contains estimates of spectrum usage, specifically, the RF received power in a specified frequency band over a networks coverage area. As a starting point for our analysis, we assume that there is a single emitter, and all sensors scan the same frequency band, where each of the sensors measures and reports the power received from the emitter. A proposed method of path loss based interpolation is simpler in terms of real-time computation by the network and it requires no knowledge of the spatial correlation of shadow fading. We also show that the estimation results come very close to those for ideal Simple Kriging.

Finally, in the concluding part, we investigates the co-existence of Wi-Fi and LTE networks in shared frequency bands. An analytical model for co-existing Wi-Fi and LTE networks is developed to evaluate the baseline performance and partially validated via experimental evaluations using USRP-based SDR platforms on the ORBIT testbed. Further, inter-network coordination with logically centralized radio resource management across Wi-Fi and LTE systems is proposed as a possible solution for improved co-existence through power and time division channel access.

Chapter 2

Performance Evaluation of Mobile Wi-Fi Hotspots in Densely Deployed Fixed Wi-Fi Networks

In this chapter, we present a study of mobile Wi-Fi wireless LAN (WLAN) hotspots which are used to provide cellular-Wi-Fi tethering service to personal devices. Mobile hotspots enable cellular users to provide Internet connectivity to multiple Wi-Fi enabled devices while on the move through Wi-Fi tethering [28, 29]. Such mobile hotspots are increasingly feasible today due to the high Internet connectivity speeds (3-6 Mbps uplink and 10-20 Mbps downlink) available through 4G/LTE cellular service [30]. According to a recent industry report [31], such mobile hotspot services are expected to increase significantly in the next 3-5 years.

Wi-Fi tethering through mobile hotspots is applicable to a variety of Wi-Fi devices, such as laptops, tablets, cameras, portable gaming systems, MP3 players, medical devices [32, 33]. Since mobile WLANs operate in the already crowded unlicensed spectrum, deployment of mobile WLANs pose potential interference problems if any fixed access points (APs) are present along the travel path of the mobile AP; one such example scenario is illustrated in Fig. 2.1(a). It is also possible that multiple mobile WLANs may interfere with each other (intra-mobile WLAN interference) as illustrated in Fig. 2.1(b). Both these interference scenarios (fixed-mobile and intra-mobile) may reduce the throughput at both, fixed and mobile APs. This motivates us to study the performance of mobile WLAN hotspots in typical urban environments which have a high density of fixed WLAN APs. The primary goal of this study is to gain a better understanding of the performance degradation experienced by mobile WLANs due to interference from fixed network APs.

A rich literature is existed on the subject of fixed AP networks, including topics such

(a) A user traveling with a mobile WLAN from point A to B can be in range of a varying number of fixed WLANs

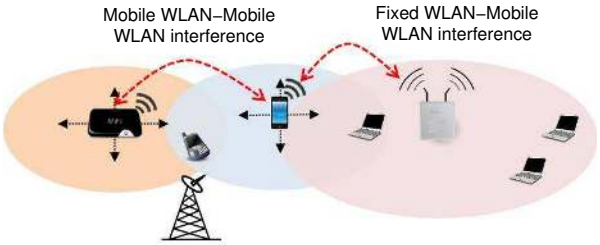

(b) Intra-mobile WLAN and mobile WLAN-fixed WLAN interference.

Figure 2.1: Co-existing scenario of fixed and mobile APs

as performance analysis of the channel sharing mechanism of 802.11 [14], effect of AP density on the client throughputs [34], and interference between overlapping managed networks [15]. In contrast, there has only been a few limited studies on mobile WLANs. In [30], the authors focus on the problem of energy efficiency for mobile hotspots, while Hare et al. studied network characteristics, usage characteristics and deployment feasibility for vehicular Wi-Fi hotspots in [35]. For quality-of-service (QoS) constrained applications using mobile hotspots, Ando et al. propose a QoS control mechanism based on TCP [36]. Here, we investigate the interaction between fixed and mobile APs; a topic which has not been explored so far.

In our simulation based study, we focus on the throughput performance of a single mobile AP co-existing with multiple fixed APs. Following unique characteristics of mobile WLANs are considered to model the interaction between mobile and fixed APs:

1. *Limited backhaul capacity at mobile APs due to limitations in 3G/4G/WiMAX*

backhaul connections. For example, 4G/LTE provides a median uplink and downlink throughput up to 6 Mbps and 13 Mbps respectively [37].

2. *Small number of clients (typically between 1 and 5) and smaller distances between AP and clients than traditional WLANs.* In contrast, commercial enterprise WLAN management techniques typically deal with large number of clients spread out at various distances from the AP locations.

3. *Dynamic nature of interference due to mobility of the AP.* Moving APs can stay in or go out of range of multiple fixed APs and/or other moving APs.

In this chapter, an analytical model for coexisting fixed and mobile WLAN hotspots with heterogeneous traffic is presented where an unsaturated traffic model for mobile APs is considered in order to reflect the limited backhaul capacity constraint. The model is used to evaluate the performance of a mobile WLAN as it transits through a set of densely deployed fixed access points (APs), and performance problems due to lack of frequency coordination are identified. An adaptive channel assignment (ACA) scheme for improving mobile AP performance is proposed and evaluated. Furthermore, we show that setting the scanning interval in ACA requires consideration of the speed at which the mobile WLAN is moving in order to compensate for the throughput losses during channel scanning.

2.1 Modeling Coexistence of Fixed and Mobile Wi-Fi APs

2.1.1 Deployment Scenario

In our MATLAB based simulation study, we consider a random deployment of multiple fixed APs in a 10 by 0.5 sq. km area. The density of APs is varied to emulate a range of real-world deployment scenarios including highways, residential, and commercial areas. A single mobile AP follows a random trajectory in the given area. We assume that each AP chooses one of the three orthogonal Wi-Fi channels in the 2.4 GHz range and the channel assignment at fixed APs is random. Also, all APs operate in the 'greenfield' or 'non-legacy support' mode of 802.11g, i.e., it assumes that there are no 802.11b devices

Table 2.1: Simulation parameters of Fixed and Mobile AP

Parameter	**Fixed AP**	**Mobile AP**
No. of APs	N	1
Traffic Model	Saturated	Unsaturated (backhaul limit: 6 Mbps)
Wi-Fi type	802.11g (green mode)	802.11g (green mode)
Parameters for 802.11g		
Channel rate	12 Mbps	54 Mbps
Header rate	6 Mbps	6 Mbps
ACK frame rate	6 Mbps	24 Mbps
σ	9μs	9μs
SIFS	10μs	10μs
DIFS	28μs	28μs
Other parameters		
MAC header	24 Bytes	
PHY header	16 Bytes	
H	PHY header @ Header bit rate, μs	
ACK	14 Bytes + PHY header @ ACK frame bit rate	
Propagation delay	1 μs	
L, length of packet	1020 Bytes @ channel bit rate, μs	
T_s	$H + L + SIFS + t_p + ACK$ $+DIFS + t_p$, μs	
T_c	$H + L + ACKTimeout$, μs	

present [38]. The carrier sense threshold of all APs is fixed at 215 meters [15]. For each fixed AP, the clients connected to it can be present at arbitrary distances; thus the channel rate cannot be assumed to be the maximum in all cases and is set to 12 Mbps for simulation purposes, considering an average case. On the other hand, clients of mobile APs are usually located in close proximity of the AP which makes possible for the AP to transmit at the maximum channel rate of 54 Mbps. Since we are primarily interested in the downlink scenarios, performance of an AP is evaluated in terms of the throughput metric. Table 2.1 summarizes the important simulation parameters used in this study.

2.1.2 Heterogeneity in Network

As mentioned earlier, mobile APs use 3G/4G/LTE connection for backhaul, for which the average download throughput is typically capped around 6 Mbps. Due to such

limited backhaul capacity, a saturated traffic model, in which the incoming packet buffer at APs always remain full, cannot be assumed for mobile APs. This leads to a heterogeneous network with a mix of saturated and unsaturated nodes when mobile and fixed APs coexist in a region [39, 40]. Malone et al. [39] presents a Markov chain model of CSMA/CA that relaxes the restriction of saturated traffic conditions given in Bianchi's model [14] and allows nodes to have any specified traffic arrival rate, λ packets/sec. We have adopted the model given in reference [39] for the mixed scenario of fixed APs (saturated node with $\lambda \to \infty$) and mobile AP (unsaturated node with $\lambda = 736$ packets/sec as per the parameters described in Table 2.1). In addition, we have modified the model to accommodate the different channel rates at fixed and mobile AP, i.e., 12 and 54 Mbps respectively. A summary of the mathematical model is as follows:

$$
\begin{aligned}
P_{tr} &= 1 - (1-\tau_1)^{n_1}(1-\tau_2)^{n_2}; \\
P_{s1} &= \frac{\tau_1(1-\tau_1)^{n_1-1}(1-\tau_2)^{n_2}}{P_{tr}}; \\
P_{s2} &= \frac{\tau_2(1-\tau_2)^{n_2-1}(1-\tau_1)^{n_1}}{P_{tr}}; \\
\mathrm{E}[S] &= (1-P_{tr})\sigma + n_1 P_{s1} P_{tr} T_{s1} + n_2 P_{s2} P_{tr} T_{s2} \\
&\quad + ((1-\tau_2)^{n2} - 1 - P_{tr} - n_1 P_{tr} P_{s1}) * T_{c1} \\
&\quad (1-(1-\tau_2)^{n_2} - n_2 P_{tr} P_{s2}) T_{c2}; \\
S_i &= \frac{P_{s_i} L_i}{\mathrm{E}[S]}; \\
S &= \sum_{i=1}^{n} S_i.
\end{aligned}
\tag{2.1}
$$

where n_i is number of APs; τ_i is probability that AP transmits in randomly chosen time slot; P_{tr} is the probability at least one AP transmits in a given time slot; P_{si} is the probability that AP of type i successfully transmits in a given time slot; $\mathrm{E}[S]$ is the expected time per slot; T_{ci} is average time that channel is busy due to collision; T_{si} is average time that channel is busy due to successful transmission; S_i is the proportion of time that the medium used by node type i for successful transmission of data; L_i is the expected time spent transmitting payload data for node type i; S is the normalized throughput of the system. Here, index i assumes the values 1 and 2 for mobile and fixed

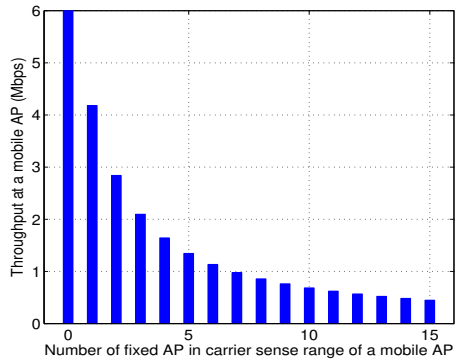

Figure 2.2: Throughput at a mobile AP as a function of number of fixed APs in the carrier sense of the mobile AP.

APs respectively. In the modified model, T_{ci} is adjusted based on the source of packets (fixed or mobile or fixed-mobile) involved in a packet collision. The notations used are consistent to those used in Bianchi's model [14]. Also, for saturation conditions at all APs ($\lambda \to \infty$), the given model reduces to Bianchi's model.

2.1.3 Performance at Mobile Wi-Fi AP

Using the given simulation parameters, we evaluate the downlink throughput performance of a single mobile AP based on a Markov chain model of CSMA/CA (refer to Eq. 5.3) as a function of the number of fixed APs $N = \{0, \ldots, 15\}$ where N fixed APs are present in carrier sense range of the mobile AP. From Fig. 2.2, it is observed that as the number of fixed APs increases, the throughput at the mobile AP decreases exponentially: from 4.18 Mbps for $N = 1$ to 0.26 Mbps for $N = 15$. We will use this preliminary results in the later sections.

2.2 Adaptive Channel Assignment

Unlike enterprise WLAN APs, commercially available mobile APs currently do not incorporate any dynamic channel adaptation schemes, possibly because of their simplified, small form-factor, and low-cost design. In this section, we study a basic frequency planning technique applicable to mobile APs, called 'Adaptive Channel Assignment' (ACA). Adaptive channel selection capability is incorporated in most fixed APs even

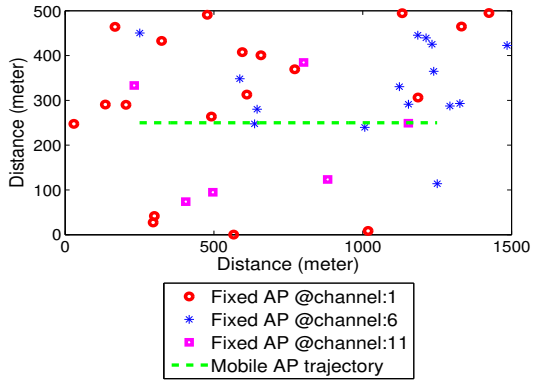

Figure 2.3: Random deployment of Fixed APs and the trajectory of the mobile AP.

though it not invoked very often; for example the popular least congested channel selection (LCCS) scheme on most Cisco-Linksys APs are only invoked when the AP is power cycled [41]. Under the ACA scheme, the mobile AP scans each channel from a candidate channel-set (here, orthogonal channels 1,6, and 11 in the 2.4 GHz band) and logs the number of unique beacons per channel. Based on the measurements, the AP changes to a less-crowded channel if the number of estimated APs on that channel is less than that of its current operating channel.

2.2.1 Increase in Throughput at Mobile Wi-Fi AP

Performance of Adaptive Channel Assignment (ACA) at a mobile AP is illustrated by considering one instance of the deployment of fixed APs as shown in Fig. 2.3. In this scenario, the mobile AP follows a specific trajectory (as per Fig. 2.3) of length 1 km with a pedestrian speed of 2 m/s. For the results presented in this section, ACA scanning and switching interval is fixed at 1 sec, but we study the effect of varying the inter-scan interval in Section 2.3. Fig. 2.4(a) and 2.4(b) show the quasi-static throughput performance of mobile APs due to ACA compared to the case when mobile APs are statically connected to one of the three Wi-Fi channels. Since ACA continuously updates the Wi-Fi channel to the one which results in the least amount of interference at the mobile AP, it shows significant improvement in the throughput performance of mobile AP over the traversed distance. Thus, we can infer that mobile

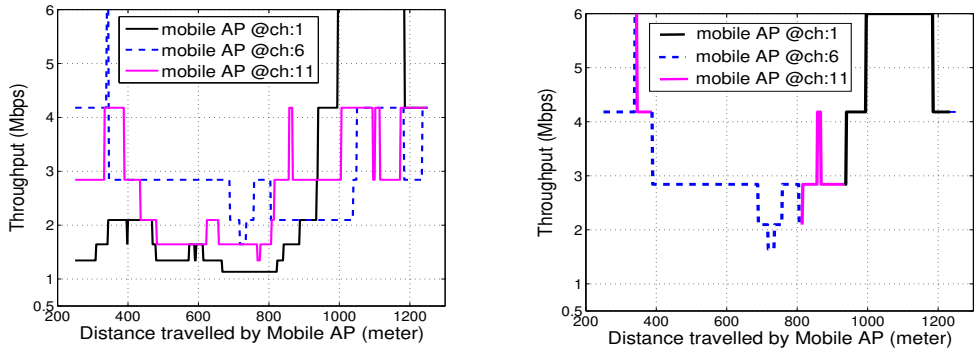

(a) Throughput at mobile AP with static channel assignment

(b) Throughput at mobile AP with ACA

Figure 2.4: Application of Adaptive Channel Assignement (ACA)

APs need frequent updates in the selection of Wi-Fi channel as they change their positions.

2.2.2 Effect of Density of Fixed W-Fi APs

The performance of mobile APs using ACA is compared with the case when a static channel is assigned at mobile APs and throughput at mobile APs is averaged over 3 possibilities of static channel assignments with varying density of fixed APs. For this simulation, we consider the same trajectory length of 1 km, and mobile speed of 2 m/s (4.5 miles/hr) as described in the Sec. 2.2.1. The number of fixed APs is varied from 10 to 120 APs/km^2. Results are calculated for $20,000$ runs of simulation for each density.

Fig 2.5(a) plots the average throughput at the mobile AP for static and adaptive channel assignments, where the throughput values are averaged over the trajectory distance. The results show that average throughput at the mobile AP with static channel assignment is in the range of 1.37 to 5.22 Mbps for the AP densities under consideration. With the application of ACA, these throughput values increase to 1.92 and 5.93 Mbps respectively, achieving a maximum gain in throughput of 1.24 Mbps. The percentage throughput increase as a function of AP density is shown in Fig.2.5(b). For lower density values, the interference offered at a mobile AP due to fixed APs is already low; thus the gain due to ACA is low as well. But as the density of fixed APs increases, interference at the mobile AP becomes significant and gains due to ACA are

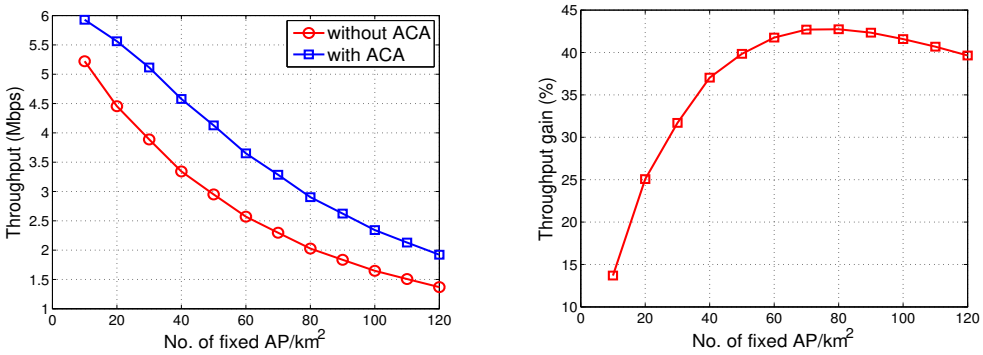

(a) Throughput (Mbps) at mobile AP with and without application of ACA

(b) Percentage improvement in throughput at mobile AP due to ACA

Figure 2.5: Increase in throughput at mobile AP due to Adaptive Channel Assignment (ACA) as a function of the number of fix APs/km^2

relatively large. The percentage gain in throughput, however saturates around 42% at the density of 70 APs/km^2. At this density, all channels are so congested that adapting the channel does not provide increasing benefit. Further increase in the density, thus results in lower gains.

2.3 Adaptive Channel Assignment with High Mobility

In Section 4.1 the throughput evaluations considered a quasi-static model where the mobile AP was considered to move at a pedestrian speed of 2 m/s. But in general, mobile APs may move with much higher speeds, especially in the case of vehicular mobile hotspots. Also, in the previous sections we showed that the frequent updates of the Wi-Fi channel can mitigate interference at mobile AP, which subsequently improves the performance at mobile AP. But this involves overheads due to channel scanning and reassignment which needs to be considered for a more accurate evaluation of the performance with ACA. The channel switching time for the 802.11 hardware chips is usually low (for example less than 1ms for the Atheros AR9462 chip [42]), but scanning multiple channels and measuring the number of beacons on each channel results in a significant overhead in the system.

During channel scanning, channel load can be estimated by two methods: (1) dwelling on each channel long enough to estimate the channel free and channel busy

fractions and (2) listening for beacons from co-channel APs. The method of load estimation depends on the sensing deployment system; thus the scanning time would vary from system to system. To simplify the analysis, we assume that the total scanning time required to estimate the load on all channels and connect on the channel with the least load is 200 ms. Since the AP cannot scan channels and transmit data at the same time, the throughput at the mobile AP is considered to be zero during this duration. For example, let us consider the earlier example where the channel was scanned for ACA every second. At this scanning interval, the average throughput at the mobile AP gets reduced by 20% because of the scanning overhead. Thus, in order to better understand this tradeoff between the throughput loss due to scanning and the throughput gain due to changing to a better channel, we measure the performance of the ACA scheme while varying the scanning period (i.e. the time period between two successive scans).

In this simulation study, the average throughput of a mobile AP is evaluated over a 10km trajectory with varying ACA channel scanning period between 1 and 20 seconds. For each value of the scanning period, the resulting throughput values are averaged over 10, 000 simulation runs. Results are plotted for four mobility speeds, s, 16.2, 32.4, 64.8 and 97.2 km/hr (10, 20, 40 and 60 miles/hr respectively) as shown in Fig. 2.6, keeping the density of fixed APs constant at 50 APs/km^2.

If ACA is not used and instead the channel assignment is done at random, average throughput at mobile AP is 2.94 Mbps. This can be considered as a baseline for comparison with ACA results with varying scanning periods. For all considered values of mobility speed, a common trend is observed for the relation between the average throughput at a mobile AP and the ACA scanning period. As the scanning period increases, the throughput at the mobile AP increases as the loss in throughput during the scanning time of 200 ms decreases. The throughput values attain a local maxima at certain values of the scanning periods (which depends on the speed of the mobile AP), and then starts a gradual decline. This reduction in throughput stems from the fact that with longer scanning periods, the mobile AP is using a non-optimal channel for longer durations.

We note that local optima of average throughput is obtained at different value of

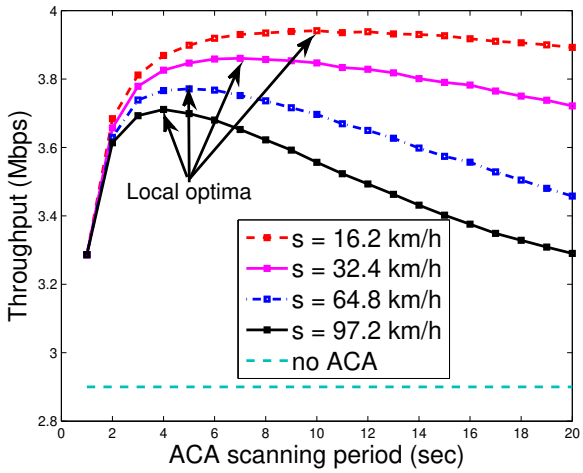

Figure 2.6: Throughput at mobile AP (Mbps) when ACA is applied, as a function of ACA scanning period (sec) for a fixed density of 50 APs/km^2

scanning interval for given values of s. For $s = \{16.2, 32.4, 64.8, 97.2\}$ km/hr, local optima is observed at scanning intervals $10, 7, 5, 4$ seconds respectively. This can be explained by the fact that at higher speeds, the mobile AP moves a greater distance between scans, each channel assignment ceases to be optimal more quickly. Thus, we conclude that scanning interval in ACA needs to be updated depending on mobility speed.

Chapter 3

Emulating Multipath Channel in Wireless Network using Equivalent Reduced Taps

Tactical radio channel simulators need to be able to accurately capture the effect of real-world wireless channels upon communication waveforms. The complexity of emulating multi-node wireless communication networks is directly related to the bandwidth of the underlying channels, and this complexity can become prohibitive to implementation when the underlying communication waveforms have bandwidths of several hundred MHz. The computational tasks needed to simulate a multi-node tactical scenario consists of two separate components: modeling the source-to-receiver channel, and modeling the impact that pairwise interference between nodes can have on the receiver's ability to demodulate transmissions. There is thus a need for techniques that can reduce the computational complexity associated with radio scenario emulation. While improving the computational cost associated with modeling the source-to-receiver channel is important, it only leads to modest gains, and it is the second case, namely modeling the aggregate effect of many other transmitters that act as interference, that can promise significant reduction in the computational complexity needed to accurately emulate a tactical radio scenario.

In this study, we consider a multi-node wireless network, either military or commercial, in which N terminals communicate dynamically in a peer-to-peer fashion, as shown in Fig. 3.1. Several nodes may communicate simultaneously over the same frequency channel, either to maximize throughput per unit bandwidth, or because the medium access protocols were not able to resolve physical interference among the transmitters. The number of taps needed to characterize any link is related to the *bandwidth-delay spread product*, which is the product of signal bandwidth (W) and the RMS delay spread

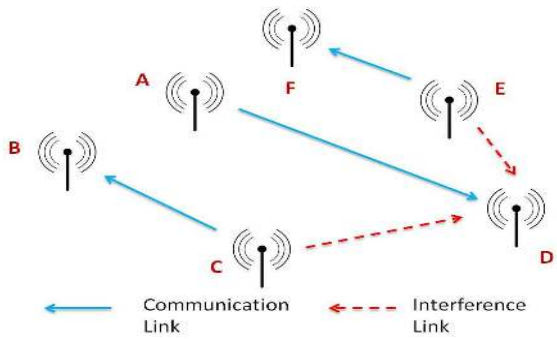

Figure 3.1: Network with $N = 6$ nodes, and three simultaneous communications links. Node D is receiving a desired signal from Node A and $M = 2$ interferers, from Nodes C and E.

(τ_{rms}) of the multipath channel. Capturing the behavior of all possible links of this network can dominate emulator cost and/or complexity. It is therefore desirable to use the least number of filter taps to represent each of the $N(N-1)$ potential links. If most links are over channels for which $W\tau_{rms}$ is large, then the number of filter taps that must be emulated, and the corresponding cost and complexity, can be prohibitively large.

In the past, several hardware and software emulators have been built to evaluate performance in such multipath scenarios [43–46], where each transmitter-to-receiver link can be a dispersive, multipath fading channel. Studies given in [46–48] emphasize challenges of computational complexity and simulation accuracy while implementing tapped-delay-line channel models on hardware. Earlier studies investigate several digital signal processing and optimization techniques. In [45], an ad hoc path combining method is proposed which employs the optimization to match total power, mean delay, and the RMS delay spread specified by the tapped-delay-line model. Borries et al. [46] proposes a scalar resolution technique in simulator modules for FPGA-based hardware simulators. Kahrs and Zimmer [48] discusses multipath signal generation based on replacing complex-valued fading functions with aggregate noise functions which can be generated by using Doppler filtering. Hoeher [49] studies the discrete-time multipath channel to compute tap-gain values using a delay-weight-and-sum method. Tap reduction schemes are employed in [50] to maximize the correlation between the band-limited

channel response functions of the estimated and reduced taps.

In our study, twofold solution based on the stochastic analysis is provided to emulate multipath channel responses - (1) firstly, 3-tap approximation to emulate direct communication link between transmitter and its intended receiver (studied in Section 3.1), and (2) n-tap approximation at interfering links to produce overall same interference channel at receiver as against emulating each interfering link individually (studied in the following Section 3.2).

3.1 Emulating Direct Communication Link using Equivalent Reduced-Tap Filters

3.1.1 Approach

Multipath channel responses occurs in wireless radio communication due to number of reasons such as physical environment (surrounding buildings, wall, hills, etc.), path geometry, frequency band and signal bandwidth. In most scenarios, they are typically represented by a multi-tapped delay line, with Rayleigh-fading tap gains, and tap spacings of $1/W$, where W is the signal bandwidth. If the RMS delay spread of the channel is τ_{rms}, the number of significant tap gains is some multiple of $W\tau_{rms}$, which can be quite large for even moderately wideband channels. Here, we assume that the channel can be characterized by a *power delay profile* (PDP) composed of a set of tap delays, $\{T_k\}$, and a set of corresponding mean-square tap gains, $\{P_k\}$, where $k = 0, 1, 2 \ldots, \hat{n}$, where $\hat{n}$ is the number of significant tap gains. Here, tap delays, $\{T_k\}$, can be arbitrarily spaced in the power delay profile. The fading statistics of the tap gains $\{P_k\}$ can be arbitrary, though here they will be assumed to be complex-Gaussian (Rayleigh fading). We will assume an exponential PDP as actual ('true') PDP that follows a widely used channel model which is described in detailed in Section **??**.

3-tap Channel Approximation

In this section, we propose tap reduction method to emulate given multipath channel which matches the PDP of channel. We investigate whether a 3-tap equivalent response

can be derived from the PDP of 'true' channel with $\hat{n} >> 1$ significant tap gains, that can be used to accurately estimate the average bit error rate, $<BER>$, vs. receiver input signal-to-noise ratio, *SNR*. The derived 3-tap PDP can be characterized by the sets of tap delays ($\{T_0, T_1, T_2\}$) and tap gains ($\{P_0, P_1, P_2\}$), where, with no loss in generality, we set $T_0 = 0$ and $P_0 = 1 - P_1 - P_2$. We present two new methods for matching the 3-tap PDP to the M-tap 'true' PDP -

1. Moment-matching approach: deriving set of $\{P_1, P_2, T_1, T_2\}$ in such a way that 3-tap PDP matches the first 4 moments of the 'true' PDP which produces excellent performance agreement up to about $W\tau_{rms} = 2$

2. Ad-hoc approach: deriving set of $\{P_1, P_2, T_1, T_2\}$ with assumption of equally spaced taps which produces excellent performance agreement for arbitrarily large values of $W\tau_{rms} > 2$.

Both approaches are explained in Section 3.1.3.

We believe the proposed solution would be of potential value to emulator design, coding of simulation platforms and analysis programs. For emulators, it simplifies the needed firmware, which leads to lower cost. Proposed scheme makes simulation coding universal where only set of input parameters $\{P_1, P_2, T_1, T_2\}$ changes based on the power delay profile of given channel. The advantage of reduced-tap responses is prominent in emulator design, especially those built for large network with multiple nodes. For a given network with N nodes, potentially, there will be $N - 1$ direct communication paths as well as $N(N - 2)$ interfering paths in a given scenario. Assuming the number of taps needed for the 'true' channel is $5W\tau_{rms}$ and the channel is only moderately wideband, e.g., $W\tau_{rms} = 2$, the proposed 3-tap approximation can cause the reduction in taps by more than 60% which leads to significant cost saving for emulators.

Notations and definitions used throughout the chapter are partly summarized in Table 3.1.

Table 3.1: Some Notations and Definitions

Bandwidth	W
Power Delay Profile as a function of delay τ	$PDP(\tau)$
RMS delay spread of the channel	τ_{rms}
longest delay among significant echoes in the channel (maximum time dispersion in the multipath channel)	τ_{max}
Gain for the kth-delayed channel echo	g_k
Power, $< \|g_k\|^2 >$, for the kth-delayed channel echo	P_k
Impulse response of the channel	$h(t)$
Ricean K-Factor	K_r
Noise Peaking Factor	NPF, y
Multipath averaged bit-error-rate	$<BER>$
Signal-to-noise ratio	SNR

3.1.2 The Exponential Channel

Here, we introduce a widely used exponential power delay profile for multipath fading channels, which we use here to represent the true channel and from which we derive a multi-tap channel impulse response. We will use this assumed true channel as baseline to develop reduced tap channel approximations in later sections.

Generic Channel Impulse Response

From Nyquist sampling theory, any linear channel of bandwidth W can be represented by a tapped delay line, with the taps spaced by $1/W$ or less. Assuming a tap spacing of $1/W$, the impulse response for such a channel can be written as

$$h(t) = \sum_{k=0}^{\hat{n}} g_k(t)\delta(t - k/W); (\text{ all channels}), \tag{3.1}$$

where $\hat{n}$ is chosen so that $\hat{n}/W$ represents the longest delay, τ_{max}, among the significant echoes in the channel; and $g_k(t)$ is the slowly time-varying complex gain for the kth-delayed channel echo which does not changes over the duration, τ_{max}, of the impulse response. The value of $\hat{n}$ should be the smallest integer equal to or greater than $W\tau_{max}$ where large $\hat{n}$ implies system implementation with more computational complexity.

Proceeding further with the general case, we now model the temporal variation, $g_k(t)$, of the gain of the kth tap. We assume that the tap gain is a Ricean process with a

Ricean K-factor, K_r. If K_r is infinite, then the tap gain is constant (nonfading channel); at the other extreme, if K_r is zero, then the tap gain is a zero-mean complex Gaussian process (Rayleigh fading channel). We will assume the latter case for purposes of this study, but the more general Ricean model for $g_k(t)$ could just as well be considered.

From the above, we can write the kth tap gain as

$$g_k(t) = (P_k)^{1/2} u_k(t); k = 0, \ldots, \hat{n}. \tag{3.2}$$

where P_k is the mean-square value of $g_k(t)$ over time (i.e., it is the average power gain of the channel echo at delay k/W); $u_k(t)$ is a complex Gaussian process of zero mean and unit variance; and each $u_k(t)$ is low-pass-filtered to have the desired Doppler spectrum. The sum of the P_k's is the average path gain, whose negative dB value is the path loss.

The Exponential Power Delay Profile

A simple way to characterize a multipath channel is through the set of power gains $\{P_k\}$, i.e., if this set is known, the impulse response in (3.1) can be determined by substituting the power gain values from this set into (3.2). A widely accepted assumption [51] is that P_k decays exponentially with increasing delay, k/W in (3.1). Then the P_k's are uniformly-spaced samples of a decaying exponential function of delay called the channel *power delay profile* (PDP). We assume the PDP has unit area and that, for the exponential case, it has the form [52–54]

$$PDP(\tau) = \frac{1}{\tau_{rms}} \exp\left(\frac{-\tau}{\tau_{rms}}\right); \tau \geq 0, \tag{3.3}$$

where τ_{rms} is the RMS delay spread of the channel.

We will model the actual channel as a tapped delay line filter, with taps spaced of $1/W$, where the kth tap gain is zero-mean and complex Gaussian with mean-square value proportional to $PDP(k/W)$, (3.3). We call this discrete PDP with exponentially decaying amplitudes the *true channel*. In using it, an amplitude scaling factor is introduced that forces the sum of the mean-square gains to be 1. In the next section, we

will describe an n-tap ($n = 3$) filter that attempts to approximate it for purposes of emulation, simulation or analysis.

Here, we note that the exponential PDP has infinite extent which, strictly speaking, makes the number of taps required to represent the channel $\hat{n} \to \infty$. The value used for $\hat{n}$ therefore depends on where the designer/analyst chooses to truncate the PDP: If the choice is to go out, e.g., to 5 times the RMS delay spread, then $\hat{n}$ will be the nearest integer for which $\hat{n}/W = 5\tau_{rms}$, i.e., $\hat{n} \approx 5W\tau_{rms}$. Including the tap at delay 0, this means that, for $W\tau_{rms} = 1$, the filter would consist of 6 taps.

3.1.3 Channel with Reduced Taps

A Moment-matching 3-tap Channel Approximation

An implementation of the tapped-delay line filter above can get large as $W\tau_{rms}$ increases significantly beyond the order of 1, corresponding to significantly greater than 6 taps. What we do here is propose a 3-tap filter that matches the true channel in such a way that the first, second, third and fourth moments of its PDP are the same as those for the true channel. It is easy to show that these four moments for the exponential profile of Eq. 3.3 are τ_{rms}, $2(\tau_{rms})^2$, $6(\tau_{rms})^3$ and $24(\tau_{rms})^4$, respectively. For a 3-tap channel, the PDP is

$$PDP(\tau) = \sum_{k=0}^{3} P_k \delta(\tau - T_k); \text{ (3-tap Channel).} \tag{3.4}$$

The design issue thus comes down to finding $\{P_k, T_k\}$ for $k = 0, 1, 2$ such that the first 4 moments of this PDP match those of the true channel's PDP. The solution must satisfy the conditions $P_0 + P_1 + P_2 = 1$ and $T_0 = 0$. Without going through the algebra, the results are as follows:

$$\begin{aligned} (P_0, T_0) &= (0.3333, 0), \\ (P_1, T_1) &= (0.6220, 1.2679\tau_{rms}), \\ (P_2, T_2) &= (0.0447, 4.7318\tau_{rms}). \end{aligned} \tag{3.5}$$

The time-varying tap gains for the filter emulation can be obtained by forming a set of independent and identically distributed (i.i.d.) complex Gaussian processes, $\{u_k(t)\}$, $k = 0, 1, 2$, that have the desired Doppler spectrum, and then applying Eq. 3.2 and

Eq. 3.19.

An Ad-hoc 3-tap Channel Approximation

We considered another plausible 3-tap channel, which is independent of the PDP moments and therefore more general. We will see, moreover, that for the PDP of Eq. 3.3 at least, it produces better performance predictions for channel with high $W\tau_{rms}$. Again subject to the conditions $T_0 = 0$ and $P_0 + P_1 + P_2 = 1$, the set of values for $\{P_k, T_k\}$ for $k = 0, 1, 2$ is

$$\begin{aligned}(P_0, T_0) &= (1/3, 0),\\ (P_1, T_1) &= (1/3, \tau_{rms}),\\ (P_2, T_2) &= (1/3, 2\tau_{rms}).\end{aligned} \tag{3.6}$$

The PDP for this channel matches that for the true channel in the first moment; almost matches it in the second moment ($1.67\tau_{rms}^2$ instead of $2\tau_{rms}^2$); and falls well short in matching the third and fourth moments. The choice of this second 3-tap channel was basically ad hoc and based on intuition.

3.1.4 Evaluation

This section describes a method to compute and compare receiver performance over the true and 3-tap channels (specifically, their bit-error-rates averaged over fading) to assess the accuracy of 3-tap equivalents as a function of bandwidth.

Evaluation Methodology

The frequency response, $H(f)$, for each of the above channel is computed by equation given as

$$H(f) = \sum_{k=0}^{\hat{n}} (P_k)^{1/2} u_k \exp(-j2\pi k f/W)$$

for the exponential channel, and similarly for the 3-tap channel.

Note that there is not one frequency response for a channel, but an infinite number, depending on the complex values chosen for the complex Gaussian, normalized tap

gains, i.e, $\{u_0, \ldots, u_{\hat{n}}\}$ for the exponential channel, and $\{u_1, u_2, u_3\}$ for the 3-tap channel. Thus, the simulation is repeated over 2000 loops to generate these sets, compute a performance metric for each set, and then get a CDF of the values computed. (Each of these 2000 trials should generate a new, independent sample of u_m at each m, so the Doppler spectrum is irrelevant for this simulation.)

Here, we compare these two kinds of channel with respect to *noise peaking factor* (NPF) which is easy to compute, and also independent of the particular modulation format, received power and noise level. NPF arises when the channel response is fully equalized, i.e., when the receiver filter is adapted to be $1/H(f)$ over the signal bandwidth (this is the *zero-forcing equalizer*). This kind of filter totally neutralizes the multipath response, but it causes an increase in the receiver output noise power. That increase is just the average of $[1/|H(f)|^2]$ over the signal bandwidth and, indeed, it requires no assumptions about the signal modulation, received power, or other link details.

By computing the NPF, denoted as y, for a few thousand realizations of the sets $\{u_0, u_1, \ldots\}$, we get a population of y-values that can be described by a CDF. Applying this procedure for both exponential and 3-tap channel, performance of 3-tap filter is analyzed to predict the NPF statistics of exponential channel.

The 3-tap approximation is further tested in terms of the multipath-averaged bit-error-rate, $<BER>$, where $<BER>$ is formulated as function of both NPF and link signal-to-noise ratio (input at the receiver), SNR. A close approximation to the instantaneous bit-error-rate, i.e., the value of BER conditioned on the value of the noise peaking factor, y, is given for the case of M-ary quadrature amplitude modulation (M-QAM) modulation by [55]

$$BER|y = 0.2 \exp\left(\frac{-1.5}{(M-1)} SNR/y\right); \tag{3.7}$$

and $<BER>$ is the bit error rate averaged over the channel realizations (in our case, the 2000 realizations of y-values generated in the above simulations). Note that SNR/y is the receiver output signal-to-noise ratio, which is diminished from its value at the receiver input (SNR) by a factor $y \geq 1$, i.e., the noise increase caused by the equalizing

filter.

For a given $W\tau_{rms}$, $<BER>$ vs. SNR curves are computed as follows:

1. For a channel type under consideration (exponential or 3-tap) and low value of $W\tau_{rms}$ (e.g., 0.5), SNR is varied in the range of 1 (0 dB) and 100 (20 dB) with the increment step of 2 dB.

2. For each SNR value, $<BER>$ is computed using the set of samples for y and Eq. 3.7.

3. Steps 1 and 2 are repeated for successive doublings of $W\tau_{rms}$.

Finally, we note that the CDF of y and the resulting curves of $<BER>$ vs. SNR depend solely on $W\tau_{rms}$. The accuracy of the 3-tap model in predicting performance is likely to decline with increasing $W\tau_{rms}$ which we evaluate in detail in the following section.

Results

As shown in Fig. 3.2, CDFs of NPF values for the exponential and moment matching 3-tap approximation channels are compared for four values of $W\tau_{rms}$. For lower values of $W\tau_{rms}$, CDFs of both the channel overlaps with each other but as $W\tau_{rms}$ increases CDFs starts separating. We see that separation between the two CDFs of NPFs becomes significant at $W\tau_{rms} = 2$. This denotes the limitation of the moment matching 3-tap approximation, i.e., the approximation may only be sufficient for $W\tau_{rms}$ up to the value where the CDF separation begins.

Results of the bit-error-rate computations for exponential and moment matching 3-tap approximation are shown in Fig. 3.3. The cases shown are $W\tau_{rms} = 1, 2, 4$ and 8, for SNR as high as 20 dB and $<BER>$ as low as 10^{-8}. The separation between exponential and 3-tap channel for a given value of $W\tau_{rms}$ determines the accuracy of the approximation. The bit-error-rate results are consistent with the previously described NPF results for which 3-tap approximation matches very closely with exponential channel when $W\tau_{rms} < 2$.

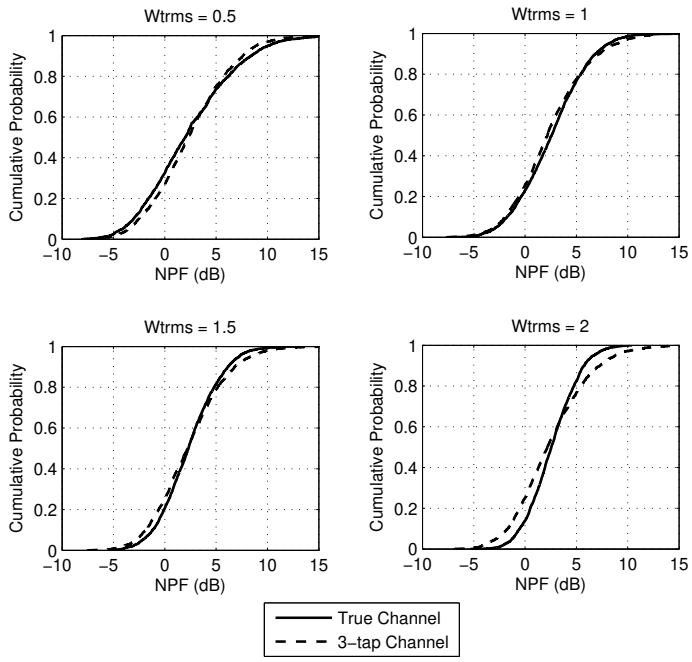

Figure 3.2: CDFs of the Noise Peaking Factor (NPF) comparing with 3-tap moment-matching channel

We quantify the accuracy of 3-tap approximation for bit-error-rate results for $W\tau_{rms} > 2$ in terms of SNR discrepancy, δ_{SNR}, which is defined as the difference between SNR values required by exponential and 3-tap approximation channel to achieve $<BER>= 10^{-8}$ (refer to Table 3.2). For $W\tau_{rms} = 2$, δ_{SNR} is less than 1 dB. As expected, δ_{SNR} increases with increase in $W\tau_{rms}$ with maximum $\delta_{SNR} = 2.7$ dB at $W\tau_{rms} = 32$. Beyond $W\tau_{rms} = 32$, δ_{SNR} seems to level off asymptotically with increasing $W\tau_{rms}$. The reason is that the variable y in Eq. 3.7 becomes more and more narrowly distributed about a single value as $W\tau_{rms}$ increases without bound. (The reason, in turn, for this narrowing is that the number of channel 'correlation bandwidths' within the signal bandwidth increases without bound, so that the random variable y converges toward its mean.)

At the more practical bit-error-rate level $<BER>= 10^{-4}$, the discrepancies are even smaller, lying below 1.5 dB. Assuming these are acceptable discrepancies in the prediction of link performance, even for signal bandwidths as high as 250 MHz, the 3-tap channel approximation can be used for RMS delay spreads up to 0.13 microseconds.

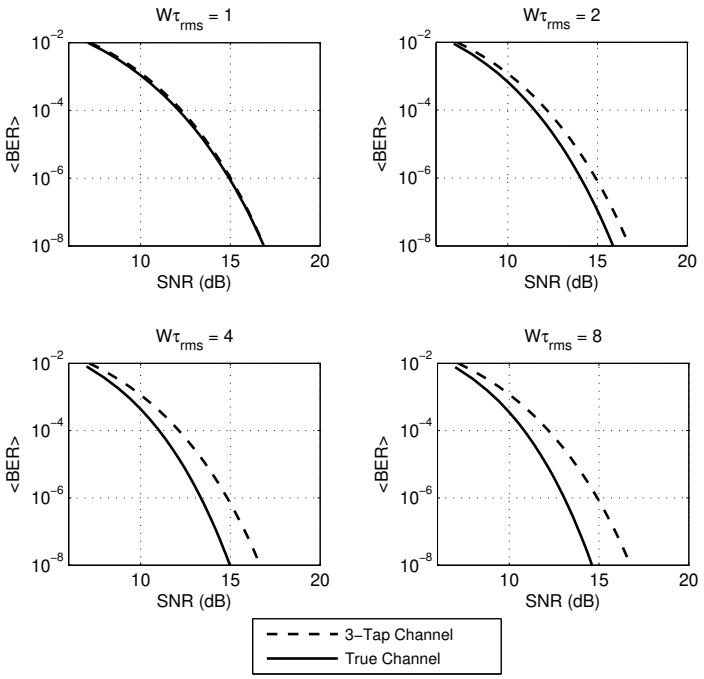

Figure 3.3: *BER* vs. *SNR* for 4-QAM Signaling comparing with 3-tap moment-matching channel

In most cases, systems with 250-MHz bandwidths will be limited to ranges so short that RMS delay spreads hardly, if ever, exceed this value.

We repeated the above exercise for the ad-hoc 3-tap channel. As given in Table 3.2, beyond the value $W\tau_{rms} = 1$, we find the discrepancies in required *SNR*, δ_{SNR}, to be smaller than for the moment-matching 3-tap channel, with minimum decrease of 25% in δ_{SNR}. As $W\tau_{rms}$ increases to very large values, the *SNR* discrepancies for $<BER>$ $= 10^{-8}$ level off at about 2.0 dB; at $<BER>= 10^{-4}$ they level off at about 1.1 dB.

Overall our 3-tap approximation analysis shows to be quite promising toward the effort of complexity reduction. For a single-carrier transmission with receiver equalization, a suitable 3-tap approximation to the true channel can be found for any combination of bandwidth and channel delay spread of likely practical interest.

Table 3.2: Discrepancies (dB) in SNR at $<BER>= 10^{-8}$

$W\tau_{rms}$	**Moment-matching 3-tap channel**	**Ad-hoc 3-tap channel**
1	0.22	0.67
2	0.91	0.22
4	1.76	0.95
8	2.06	1.42
16	2.46	1.75
32	2.69	1.94
64	2.64	2.04
128	2.61	1.91

3.2 Emulating Co-Channel Interference Using Equivalent Reduced-Tap Filters

In Section 3.1, we see that the multipath channel responses for each channel link can be represented by equivalent reduced-tap filters. But in multinode wireless network, there are a number of interfering links, so their emulation complexity, could become dominant when multiple communication links are active simultaneously on the same channel. The number of filter taps required per link to emulate the actual channel is a function of the channel bandwidth W and RMS delay spread τ_{rms}. Assuming each per-link channel to have an exponentially decaying power delay profile, this value is about $4W\tau_{rms}$. We propose to emulate each link using n uniformly-spaced taps of equal mean-square gain in such a way that overall received interference can be represented by combining the n-tap multipath responses at the interfering links. In our case, the required number of taps to emulate per-link channel is only $2W\tau_{rms}$, while maintaining the important characteristic (i.e., the CDF of total power, taken over the fading) of the actual (exponential) channel. We derive this result analytically and confirm it by simulation. Improving on this 50% reduction in required taps, we further show that the loss in accuracy is significantly low so long as the total number of taps emulated is the order of 16 or more. For large values of $W\tau_{rms}$, this can lead to even more reduction in n and, thus, further limit the cost and complexity of emulators.

3.2.1 Approach

To estimate the number of taps, n, needed per link, we consider the following scenario: There are $M < N$ interference signals at a given receiver, all having the same multipath-averaged power; all M signals are received over channels with exponential *power delay profiles* (PDPs); the M channels have independent fading and the same $W\tau_{rms}$; and each channel is represented by a filter with n taps of equal mean-square gain. Our goal is to determine the total number of per-link filter taps, n, needed for a given M and $W\tau_{rms}$, such that the CDF of total instantaneous received interference power, taken over the ensemble of all channel fades, is essentially the same as that for the true (exponential) PDP. We use a combination of analysis and simulation to obtain the required n. We show that, for any M, a very close CDF fit is obtained whenever n is twice $W\tau_{rms}$. To implement the true (exponential) channel would require, instead, 3 or 4 times this product, so the proposed emulator approach would yield a tap reduction of up to 50%. Furthermore, when the product nM equals or exceeds the order of 16, the inaccuracy in using the emulator to assess interference is small for any $W\tau_{rms}$. For wideband channels, where $W\tau_{rms}$ is large, this would permit even greater reductions, both in the total number of required taps and in the number of required taps per link. Notations and definitions used throughout this chapter are summarized in Table 3.3.

3.2.2 The Exponential Interference Channel

The 'true' response of the links over which the interfering signals propagate is represented by an exponential discrete *power delay profile* (PDP) as explained in previous Section 3.1.2. In this section, we further derive the instantaneous total interference power for this channel and derive its mean and variance over the multipath fadings of the M links. In using the channel with exponentially decaying amplitudes, an amplitude scaling factor is introduced that forces the sum of the mean-square gains to be 1 (see Section 3.2.2).

Table 3.3: Some Notations and Definitions

Number of active nodes in the network	N
Number of interfering links	M, $M < N$
Power Delay Profile as a function of delay τ	$PDP(\tau)$
Bandwidth	W
RMS delay spread of the channel	τ_{rms}
Bandwidth-delay spread product	$W\tau_{rms}$
Mean power for the kth-delayed channel echo	P_k
Number of PDP rays per link for true channel	$\hat{n}$
Number of PDP rays per link for approximated channel	n
Power spectrum density of the transmitted signal	$S(f)$
Power spectrum density of the received signals	$S_{rec}(f)$
Frequency response of the channel	$H(f)$
Instantaneous power received from a single interfering link	y
Instantaneous power received from M interfering links	z

Total Instantaneous Interference Power

Assume there are M interfering links, all having the same transmitted power spectral density, $S(f)$, and the same mean-square path loss, G, to the receiver of the desired signal. For convenience, we set $G = 1$. The power spectral density of a single interfering signal at the receiver is

$$S_{rec}(f) = S(f)|H(f)|^2; 0 \leq f \leq W, \tag{3.8}$$

where $H(f)$ is a random multipath fading response whose mean-square value at every f is 1. For the case of $\hat{n}$-taps (multi-ray PDP), $H(f)$ can be written as

$$H(f) = \sum_{k=0}^{\infty} P_k^{1/2} u_k \exp(-j2\pi fk/W). \tag{3.9}$$

where k/W is relative delay; P_k is the mean power in the kth ray; all the u_k are independent and each u_k is a slowly time-varying complex Gaussian random process. It fluctuates at a rate comparable to the Doppler bandwidth, which is very small compared to the fluctuation rate of the signal (on the scale of the bandwidth, W). Thus, we can

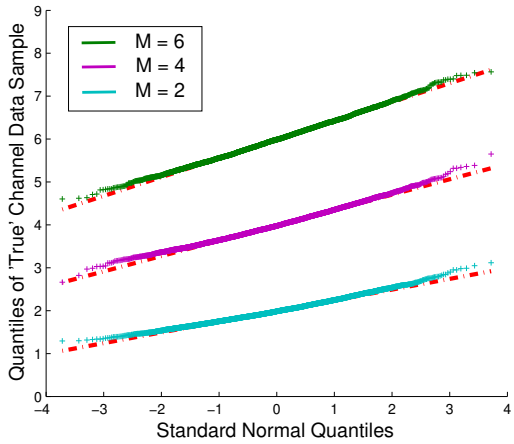

Figure 3.4: Quantile-quantile plots of z for an exponential PDP with $W\tau_{rms} = 16$ and $M = 2, 4, 6$. For each M, the plot shows the closeness of z to a Gaussian variable of the same mean and variance (red dashed line).

regard $H(f)$ in (3.9) as quasi-static, but still a random function that will vary over time.

The power in the received signal (conditioned on the u_k) from the given interfering link is the integral of $S_{rec}(f)$, (3.8), over the signal bandwidth. We can assume that $S(f)$ is uniform over the signal bandwidth, as in the most modern radio systems. For simplicity and with no loss in generality, we assume that the uniform value is $1/W$, so that the total transmit power is 1. Thus, $S_{rec}(f)$ simplifies to the integration of $|H(f)|^2$ over the bandwidth W. As taps are spaced at integer multiples of $1/W$, the integral of $|H(f)|^2$ reduces to the sum of the ray powers. Thus, instantaneous power received from one interfering link, y, over a multipath channel with an exponential power delay profile is given by

$$y = \int_f (1/W)|H(f)|^2 \mathrm{d}f = \sum_{k=0}^{\infty} P_k |u_k|^2. \tag{3.10}$$

We assume that each interference link has an independent channel response. Thus, the total instantaneous power, z, of the received interference from M links is the sum of M independent and identically distributed (i.i.d.) variables like y.

Analysis of the Exponential PDP

Each normalized path gain for each interference link (e.g., each u_k in (3.10)) is a zero-mean, unit-variance, complex Gaussian fading term. Thus, $|u_k|^2$ is a random variable whose pdf is a decaying exponential of unit mean. We have learned that, as $W\tau_{rms}$ grows large, the pdf of z tends towards a near-Gaussian distribution. For example, Fig. 3.4 compares quantile-quantile plots of the variable z against those of a Gaussian variable with the same mean and variance; the closeness of each solid curve to the straight dashed line beneath it confirms that z is near-Gaussian for the conditions shown. For the n-tap channel with uniform mean-square gains, the same will be true as n grows large. Therefore, the CDF of total fading power for the two kinds of channels will be very similar so long as y has the same mean and variance for both [56]. This motivates us to (i) derive the mean and variance of z for the exponential PDP; (ii) do the same for the n-tap PDP; and (iii) equate the moments to obtain n as a function of $W\tau_{rms}$. We complete Step (i) here.

To begin, the expression for P_k is given as

$$P_k = \frac{A}{W\tau_{rms}} \exp\left(\frac{-k}{W\tau_{rms}}\right);\ k = 0, \ldots, \infty, \tag{3.11}$$

where the factor $1/W$ is added to average $|H(f)|^2$ over frequency in a bandwidth W; and A is chosen so that the infinite sum over k is 1. Using $\sum_k x^k = 1/(1-x)$ for $0 < x < 1$ and $k = 0, 1, \ldots, \infty$, we have

$$A = W\tau_{rms}\left(1 - \exp\left(-1/W\tau_{rms}\right)\right),$$

which gives P_k as

$$P_k = \left(1 - \exp\left(\frac{-1}{W\tau_{rms}}\right)\right) \exp\left(\frac{-k}{W\tau_{rms}}\right);\ k = 0, \ldots, \infty. \tag{3.12}$$

We note that, for very large $W\tau_{rms}$, A approaches 1.

Due to the specific assignment of A here, we have $\mathrm{E}[y] = 1$; thus, $\mathrm{E}[z] = M$. Variance of y, $\mathrm{var}\{y\} = \mathrm{E}[y^2] - \mathrm{E}[y]^2$, requires its first and second moments where we

already know that the first moment is 1. Now, with reference to (3.10),

$$\begin{aligned} \mathrm{E}[y^2] &= \textstyle\sum_k P_k^2 \mathrm{E}[|u_k|^4] + \sum_k \sum_{j \neq k} P_j P_k \mathrm{E}[|u_j|^2 |u_k|^2]; \\ & \qquad\qquad\qquad\qquad\qquad\qquad j, k = 0, \ldots, \infty. \end{aligned} \tag{3.13}$$

The mean of $|u_j|^2|u_k|^2$ can be evaluated considering the two cases $j = k$ and $j \neq k$.

Case: $k = j$

Since each u_k is a zero-mean, unit-variance, complex Gaussian, $x = |u_k|^2$ is an exponential random variate (r.v.) of unit mean with pdf $P_X(x) = \exp(-x); x > 0$. Thus,

$$\mathrm{E}[|u_k|^4] = 2.$$

Case: $k \neq j$

Here, $x_k = |u_k|^2$ and $x_j = |u_j|^2$ are independent exponential random variable with joint pdf $P_{X_k,X_j}(x_k, x_j) = \exp(-x_k)\exp(-x_j); x_k > 0, x_j > 0;$

$$\mathrm{E}[|u_j|^2|u_k|^2] = 1.$$

Thus, (3.13) simplifies to

$$\mathrm{E}[y^2] = \sum_{k=0}^{\infty} P_k^2 + \sum_{k=0}^{\infty}\sum_{j=0}^{\infty} P_j P_k. \tag{3.14}$$

As P_k^2 and $P_j P_k$ are known functions of $W\tau_{rms}$, we can get closed form expressions for these sums as

$$\begin{aligned} \sum_{k=0}^{\infty} P_k^2 &= \frac{1 - \exp(-1/W\tau_{rms})}{1 + \exp(-1/W\tau_{rms})}; \\ \sum_{k=0}^{\infty}\sum_{j=0}^{\infty} P_k P_j &= 1. \end{aligned} \tag{3.15}$$

From (3.14) and (3.15), an expression for $\mathrm{var}\{y\}$ is given by

$$\mathrm{var}\{y\} = \frac{1 - \exp(-1/W\tau_{rms})}{1 + \exp(-1/W\tau_{rms})}, \tag{3.16}$$

and final expressions for mean and variance of total instantaneous interference power z

are given by

$$\begin{aligned} \mathrm{E}[z] &= M\mathrm{E}[y] = M; \\ \mathrm{var}\{z\} = M\mathrm{var}\{y\} &= M\frac{1-\exp(-1/W\tau_{rms})}{1+\exp(-1/W\tau_{rms})}. \end{aligned} \tag{3.17}$$

Finally, we note that for simulation/evaluation purpose, one might choose to truncate the PDP to 4 or 5 times the RMS delay spread. Assuming the latter, $\hat{n}$ will be the nearest integer for which $\hat{n}/W = 5\tau_{rms}$, i.e., $\hat{n} \approx 5W\tau_{rms}$. Including the tap at delay 0, this means that, for $W\tau_{rms} = 1$, the filter would consist of 6 taps.

3.2.3 Emulator Channel with Reduced Taps

This section introduces the response of the channels to be emulated, each being an n-tap response with uniform mean-square tap gains. We derive the mean and variance of total interference power for this channel as well and, by equating them with those for the exponential channel, we determine the required n as a function of $W\tau_{rms}$.

The n-tap Channel Approximation

An implementation of the tapped-delay line filter above can get large as $W\tau_{rms}$ increases significantly beyond the order of 1, corresponding to significantly more than 6 taps. We propose here an n-tap filter ($n < \hat{n}$) having the PDP

$$PDP(\tau) = \sum_{k=0}^{n-1} P_k \delta(\tau - T_k), \tag{3.18}$$

where PDP is subject to the conditions $T_0 = 0$ and $P_0 + P_1 + \ldots + P_{n-1} = 1$; and the set of values for $\{P_k, T_k\}$ for $k = 0, 1, \ldots, n-1$ is

$$\begin{aligned} P_k &= 1/n, \\ T_k &= 2k/W. \end{aligned} \tag{3.19}$$

The time-varying tap gains for the filter emulation can be obtained by forming a set of i.i.d. complex Gaussian processes, $\{u_k(t)\}$, $k = 0, 1, \ldots, n-1$, that have the desired Doppler spectrum, and then applying (3.2). We will see that, with the above choices of

tap amplitudes and spacings, an n can be found which gives excellent agreement with the exponential PDP, both in the CDF of total interference power and in the RMS delay spread.

Analysis of the n-tap PDP

The spectral analysis of instantaneous interference power, leading to (3.10) for the instantaneous power sum, y, in an interference link, is the same for the n-tap channel. Thus we can write

$$y = \sum_{k=0}^{n-1} (1/n)|u_k|^2. \tag{3.20}$$

Since $x = |u_k|^2$ is an exponential random variate (r.v.) with pdf $P_X(x) = \exp(-x); x > 0$, the sum, v, of n unit-mean r.v.'s is an nth-order Gamma r.v. with pdf

$$P_V(v) = \frac{v^{n-1}\exp(-v)}{(n-1)!}; v > 0. \tag{3.21}$$

From (3.20), the received power y is v/n so that we have

$$P_Y(y) = nP_V(v = ny) = \frac{n^n y^{n-1}\exp(-ny)}{(n-1)!}; y > 0, \tag{3.22}$$

which indicates the pdf of the received power, y, due to one interferer. However, there are M such interfering links and, according to our assumptions, they are all i.i.d. Therefore, z is a sum of $n' = nM$ i.i.d. exponential r.v.'s, each having a mean of $1/n$. We thus obtain the pdf of z as

$$P_Z(z) = \frac{n^{n'} z^{n'-1}\exp(-nz)}{(n'-1)!}; z > 0. \tag{3.23}$$

Here, z represents the total instantaneous interference power due to M interfering links and has mean and variance

$$\mathrm{E}[z] = \frac{n'}{n} = M; \mathrm{var}\{z\} = \frac{M}{n}. \tag{3.24}$$

Table 3.4: Number of taps n as a function of $W\tau_{rms}$

$W\tau_{rms}$	n (Eq. (3.25))	n (Eq. (3.26))
0.5	1.31	1
0.75	1.72	2
1	2.16	2
2	4.08	4
3	6.06	6
4	8.04	8
8	16.02	8
16	32.01	8
32	64.005	64

Required Number of Taps Per Link, n

We now combine (3.17) and (3.24) to match the moments, E[z] and var{z}, for the two kinds of channels. The means for the two cases are automatically matched because of our normalizations. Now equating the variances, we obtain

$$n = \frac{1 + \exp(-1/W\tau_{rms})}{1 - \exp(-1/W\tau_{rms})} = \coth\left(\frac{1}{2W\tau_{rms}}\right) \tag{3.25}$$

which shows n to be a function of the bandwidth-delay product $W\tau_{rms}$ only. If n is not an integer, it can be chosen equal to the integer nearest to the formula (but never less than 1). For example, for $W\tau_{rms} = 0.5$, $n = 1$ tap; for $W\tau_{trms} = 0.75$ and 1.0, $n = 2$ taps; and so on (refer to Table to 3.4). Also, it is observed that as $W\tau_{rms}$ increases n approaches value $2W\tau_{rms}$. In light of these observations, we can write a simple-yet-accurate approximation for n, namely,

$$n = Q(\max(1, 2W\tau_{rms})), \tag{3.26}$$

where $Q(x)$ means "quantization of x to the nearest integer". The closeness of (3.25) and (3.26) can be discerned from Fig. (3.5).

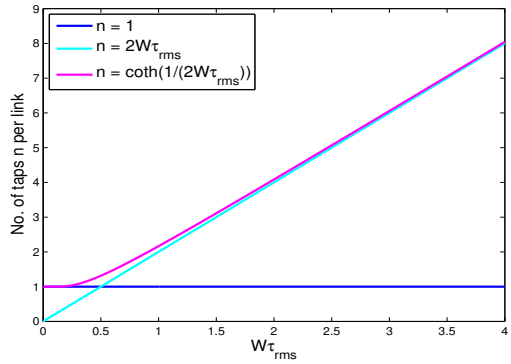

Figure 3.5: Number of taps n per link: Comparison of $n = \coth(1/(2W\tau_{rms}))$ from analysis $n =$(Max$(1, 2 * W\tau_{rms})$)

3.2.4 Results

The n-tap Channel Approximation

Figure 3.6 shows CDFs of total interference power, z, for each of four values of $W\tau_{rms}$, namely $1, 2, 4, 8$. For each such value, curves are shown for three values of $M = 2, 4, 6$. Each curve seen there are actually two curves overlapped, one for the exponential PDP and the other for the n-tap PDP with n given by (3.26). The CDF for the approximated (n-tap) channel matches that for the exponential channel, for each given M and $W\tau_{rms}$. This confirms the validity of the n-tap channel approximation.

Another issue is the RMS delay spreads for the two kinds of PDPs. Given the tap spacing of $2/W$ for the n-tap channel, we computed RMS delay spread for $W\tau_{rms}$ values from 1 to infinity. The result is that, over that range, the RMS delay spread for the n-tap channel increased from τ_{rms} (the RMS delay spread for the exponential PDP) to $1.155\tau_{rms}$, a deviation never greater than 16%.

Some intuitive aspects are worth noting: For $W\tau_{rms} < 0.5$, our formula, (3.26) specifies only one tap. For this condition, the channel is essentially flat-fading (little or no frequency selectivity), so $n = 1$ is an intuitively obvious solution. We can also see that the delay span of the n-tap response ranges from $2\tau_{rms}$ (for $W\tau_{rms} = 1$) to $4\tau_{rms}$ (as $W\tau_{rms}$ goes to infinity). This is intuitively satisfying: it suggests that the n-tap response covers the most significant part of the response of the 'true' channel's

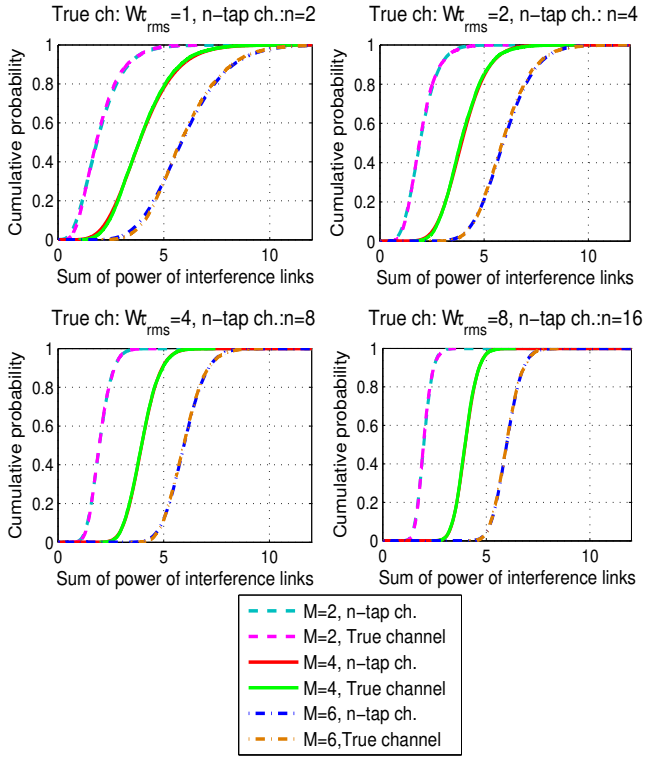

Figure 3.6: CDFs of z for n-tap channel and true (exponential) channel, when the number of interfering links is $M = 2, 4, 6$ and $n = 2W\tau_{rms}$.

exponential PDP.

An Alternative Approach for $Mn \geq 16$

There is an alternative way of looking at this problem that leads to an even less stringent requirement on the number of taps. It begins with the observation that, for many studies, the model of interference must merely be accurate up to some high level of interference, e.g., up to the 95th percentile. With that in mind, we note that the CDF of z becomes very steep (i.e., becomes more step-like) as as the total number of emulator taps increases to large values. For combinations of M and $W\tau_{rms}$ where $n' = Mn$ is on the order of 16 or greater, we find that the CDFs for both channels are so steep that their 95th percentiles of total power are no more than 1 dB apart. Thus, as M and $W\tau_{rms}$ increase, $n' = Mn$ need not be bound by the prescription $n = 2W\tau_{rms}$; n can be smaller, so long as Mn is 16 or greater, leading to even greater savings in the

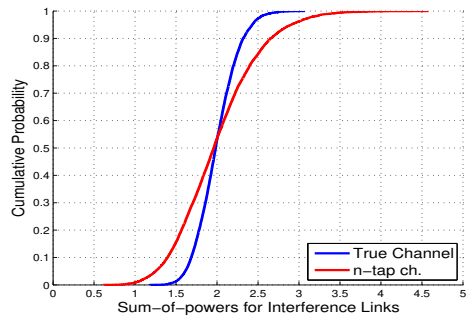

Figure 3.7: CDFs of z for n-tap channel approximation with $n = 8$ in comparison with an exponential PDP with $W\tau_{rms} = 16$ for interfering links $M = 2$.

number of emulator taps. We can express this analytically by the prescription

$$\begin{aligned} n &= \min(2W\tau_{rms}, 16/M); \\ n' &= \min(2MW\tau_{rms}, 16). \end{aligned} \tag{3.27}$$

As an example, consider the realistic case of two interfering links ($M = 2$) and an exponential PDP with $W\tau_{rms} = 16$. Using the more conventional approach, the $1/W$-spaced channel taps used for each interference link would span a delay interval $\sim 4\tau_{rms}$. Hence, the number of taps per link would be $\sim 4W\tau_{rms} = 64$; and for $M = 2$, the total would be 128. The above analysis shows that an emulator with a total of 16 taps (8 per link) would suffice to capture the statistics of the total interference power, a reduction in the total and per-link numbers of taps of $8 : 1$.

The CDFs of total power for the two channels in this case are shown in Fig. 3.7. Since n is not $2W\tau_{rms}$, as prescribed in (3.26), the CDFs do not lie on top of each other (as in Fig. 3.6). However, they are only 0.8 dB apart at the 95% level. In studying the impact of interference, the effect of this inaccuracy would be trivial.

Chapter 4

Practical Interpolation for Spectrum Cartography through Local Path Loss Modeling

4.1 Radio Mapping Approach

The mapping approach described here exploits the mathematical structure of most terrestrial path loss models, which are based on numerous measurement and modeling campaigns over many years. To be specific, the majority of path loss models published for outdoor environments are of the form $PL(d) = B + \Gamma log(d/d_r) + S$, where B and Γ are constants that depend on frequency, antenna heights and gains, and terrain details; S is the statistical variation of path loss about $[B + \Gamma log(d/d_r)]$ over all Tx-Rx separations of distance d. Here, d_r is a reference distance, which we will assume, for convenience only, to be 1 m. Path loss models having this form can be found, for example, in [57–62]. It is customary to regard $[B + \Gamma log(d/d_r)]$ as the median path loss for distance d, and S as shadow fading, typically modeled as a zero-mean Gaussian random process over the environment. Finally, the received power at a given point on the terrain can be written as, $P_r = P_t + PL(d)$, which is the quantity to be mapped. Here, P_r corresponds to receive power, and P_t is the transmit power. Invoking the generic path loss form assumed here, P_r is

$$P_r = A + \Gamma \log(d/d_r) + S, \tag{4.1}$$

where $A = P_t + B$.

The constants A and Γ are context-specific in that they depend on the transmitted power and the terrain features over the areas to be mapped. In an environment filled with sensors, they can be computed by the network for any small (local) area by

measuring received power at n nearby sensors and performing least-squares estimation (LSE) or other forms of estimation [63,64][1]. With A and Γ thus quantified, the median received power

$$P_m = A + \Gamma \log(d/d_r). \tag{4.2}$$

can then be computed for any given point within the local area, and thus only S needs to be further estimated at that location of interest. This can be achieved by measuring S at each of the n nearby sensors (i.e., by subtracting the median at the sensor from the measured power) and then forming an n-fold weighted sum of the resulting S-estimates. This is the essence of our approach, which we describe in detail in later sections, and can be applied to any and all points within the coverage area to create the radio map.

For finite n, the estimates of A and Γ will be imperfect due to the corrupting effects of the random shadow fading, with the estimates tending to improve as n increases. We require that $n > 2$ in all cases and later in this paper will examine a specific scenario wherein $n = 4$. We will also propose a simple weighting scheme for estimating S at a given point (which yields a powerful variant of inverse distance weighting, IDW) that does not require knowing the spatial statistics of shadow fading; and we will see that, in terms of RF power estimation accuracy, the results are close to a best-case bound, which we will derive.

4.2 The Stochastic Method

In this section, we present the heart of our approach to performing the underlying interpolations associated with estimating received power. We start by first providing a quick background discussion regarding the spatial characteristics of shadow fading, then move to presenting the idealized form of our interpolation approach, which includes analyzing the first and second moments of shadow fading at an arbitrary point.

[1]Throughout this study we shall explore the use of least-squares estimation, due to its combination of simplicity and good performance, but note that our methodology can apply equally well to other approaches, such as maximum-likelihood estimation.

4.2.1 Spatial Correlation of Shadow Fading

The interpolation approach that we will describe will involve: (i) using in-field measurements to estimate the 'deterministic' part of P_r at a given point; and (ii) focus on estimating the 'random' part, S, at the point of interest. One can envision the shadow fading component as a two-dimensional stochastic process over the terrain, where S at any point is a Gaussian random variable of zero mean and standard deviation σ; and the relationship between S-values at any two points i and j can be characterized by an autocorrelation function,

$$< S_i S_j >= c_{ij}, \tag{4.3}$$

where $< X >$ denotes the expected value of X. The optimal way to estimate S at a location between measurement points (sensors) is to know and exploit the correlation properties of S over the terrain, and hence we call this the stochastic method (SM).

A popular formulation for c_{ij} that is simple to use and supported by data in the literature [65], is the decaying exponential,

$$c_{ij} = \sigma^2 \exp\left(-\frac{d_{ij}}{X_c}\right), \tag{4.4}$$

where d_{ij} is the physical distance between points i and j, and X_c is the so-called correlation distance of shadow fading on the terrain. The value of this parameter depends on the type of terrain, and empirical results have been reported for different environments [66–68].

In our computations of RMS interpolation error, we will invoke the above correlation coefficient as well as others, showing that the precise shape of the function is not a first-order concern in the underlying problem.

4.2.2 The Ideal Case: SM-0

Assume that P_r is to be estimated at a given point on the terrain (labeled as point 0), which is surrounded by n measuring sensors ($n > 2$). The parameters A and Γ are estimated from the n measurements of received power, and will be imperfect estimates

due to the S-values, which act like additive noise. To obtain a theoretical best-case accuracy, however, we assume at first that these estimates are perfect. Therefore, the median value of P_r at point 0 is exact, and the network need only predict S_0 (S at point 0). To quantify the minimal RMS error in this prediction, we use the mathematics of multivariate Gaussian distributions: Assuming that $S_1, .., S_n$ are measured precisely at the sensors, S_0 is modeled as

$$[S_0|S_1, .., S_n] \simeq \mu_0 + \sigma_0 u, \tag{4.5}$$

where μ_0 is the mean of S_0 conditioned on $S_1, .., S_n$ and is a weighted sum over these S-values; u is a zero-mean, unit-variance Gaussian random variate; and σ_0 is the standard deviation of the variation about the mean. We will show that the weights over the n S-values can be determined if its correlation is known. Thus, in the ideal case, the expected value of S_0 can be known, in addition to the median of P_r. This leaves only $\sigma_0 u$ as the unknowable component of P_r. Thus, σ_0 is the irreducible RMS error in interpolating P_r from the sensor measurements.

It is worth noting that the above approach is equivalent to a basic form of Kriging, which is often referred to as Simple Kriging [69]. We show in Section **??** of the Appendix that the minimum RMS error is equivalent to the RMS error obtained from Simple Kriging, where the bias term is precisely known.

4.2.3 Determining μ_0 and σ_0

For the ideal case, SM-0, the environmental parameters A, Γ, and shadow fading values at n sensors are perfectly known. Thus, $P_{r,0}$ at point 0 is given as

$$P_{r,0} = A + \Gamma \log(d_0/d_r) + [\mu_0 + \sigma_0 u], \tag{4.6}$$

where d_0 is the distance from point 0 to the emitter, and the bracketed term corresponds to the shadow fading component, (4.5).

Under the ideal conditions assumed, we can determine μ_0 and σ_0 exactly, since

Table 4.1: Notation description

Notation	**Parameter**
n	Number of sensors
$A^{"}$	Redefined path loss constant
γ	Path loss exponent
$P_{r,i}$	True measurement (received power) at i
$P_{m,i}$	True median power at i
σ	Standard deviation of shadow fading
X_c	Shadow fading correlation distance
S_i	True shadow fading at i
$\boldsymbol{W}$	Weights vector assigned to sensor measurements
d_i	distance between emitter and i
SM	Stochastic Method
RMSE	Root Mean Square Error

$\mathbf{S} = [S_1, \cdots, S_n]$ is an n-fold set of zero-mean Gaussian variates of known correlation matrix. The joint probability density function (pdf) of this set is [70]

$$f_S(s) = ((2\pi)^n |\boldsymbol{C_n}|)^{-1/2} \exp\left(-\frac{1}{2}(\boldsymbol{S^T C_n S})\right) \tag{4.7}$$

where $\boldsymbol{C_n}$ is $n \times n$ correlation matrix of $\boldsymbol{S}$ with determinant $|\boldsymbol{C_n}|$ and each of its elements is computed by (4.3). Thus, from multivariate Gaussian statistics [71], $[S_0|\mathbf{S}]$ has mean μ_0 and standard deviation σ_0 given by

$$\begin{aligned} \mu_0 &= (\boldsymbol{c_0^T C_n^{-1}})\boldsymbol{S}, \\ \sigma_0^2 &= \sigma^2 - \boldsymbol{c_0^T C_n^{-1} c_0}, \end{aligned} \tag{4.8}$$

respectively, where $\boldsymbol{c_0}$ is the $n \times 1$ cross-correlation vector of S_0 with $\boldsymbol{S}$, where the j-th element is given as $c_0(j) =< S_0 S_j >$. From (4.8), we see that μ_0 is a weighted sum over the S-values at the n sensors, $\mu_0 = \boldsymbol{W^T S}$, where the weight vector is

$$\boldsymbol{W} = (\boldsymbol{c_0^T C_n^{-1}})^{\boldsymbol{T}}. \tag{4.9}$$

Table 4.1 lists notations which we have used here and in the rest of the study.

4.3 Reducing the Stochastic Method to Practice

Examining the SM-0 approach suggests several ways to reduce the processing to practice. This is important because: (i) in reality, the median power cannot be known precisely; (ii) it is very difficult to determine the correlations c_{ij} and, thus, the correlation matrices $\boldsymbol{C_n}$ and $\boldsymbol{c_0}$; and (iii) even if it can be done, the real-time computation needed to obtain the weights for estimating μ_0 can be quite high, especially as n increases.

In this section, we present and analyze a more realizable approach, SM-1, which addresses the first concern about the median power; and following that, we present SM-2, which is slightly less ideal than SM-1 but addresses all three issues.

4.3.1 The First Method, SM-1

For convenience, we begin by rewriting the power measured at the i-th sensor, where we assign $d_r = 1$ m, and we express Γ as 10γ, where γ is the path loss exponent. We assume, moreover, that $i = 1, .., n$ where n is the number of sensors whose measurements are used to predict power at a particular unmeasured point (point 0). The power received at the i-th sensor is rewritten as

$$\begin{aligned} P_{r,i} &= A + 10\gamma \log d_i + S_i,\ i = 1, .., n, \\ &= (A + Z_n) + 10\gamma \log d_i + (S_i - Z_n), \end{aligned} \tag{4.10}$$

where

$$Z_n = \frac{1}{n} \sum_{i=1}^{n} S_i. \tag{4.11}$$

i.e., Z_n is the average of the S-values at the n sensors. The reason for this reformulation will be made clear shortly.

A general approach to reducing the stochastic method to practice is as follows:

1. Use the n measured values of $P_{r,i}$, along with least squares estimation (LSE), to estimate $A + Z_n$ and γ, leading to estimates, $A^{'}$ and $\gamma^{'}$, that are imperfect. Due to the normal distribution of shadow fading values, the received power is also

normally distributed with mean P_m, the median received power, and variance σ^2. In this case, LSE is equivalent to maximum likelihood estimation [72].

2. Use the estimates $A^{'}$ and $\gamma^{'}$ to estimate the shadow fading term at each sensor, i.e.,

$$S_i^{'} = P_{r,i} - (A^{'} + 10\gamma^{'} \log d_i). \tag{4.12}$$

3. To estimate $P_{r,0}$ at point 0, use the equation

$$P_{r,0}^{'} = A^{'} + 10\gamma^{'} \log d_0 + S_0^{'}. \tag{4.13}$$

where d_0 is the distance from the emitter to point 0, and $S_0^{'}$ is a weighted sum over the n estimates, $S_1^{'}, S_2^{'}, .., S_n^{'}$. The weights $w_1, w_2, .., w_n$ are the elements of $\boldsymbol{W}$, (4.9).

What we call SM-1 is this three-step approach, which requires knowing the spatial correlation matrix of shadow fading; the second reduction method to be discussed later, SM-2, uses an ad hoc weighting approach that requires no such knowledge.

The reformulation of the power equation, (4.10), can now be explained: Conditioned on the n values of S_i, the LSE algorithm seeks a solution $(A^{'}, \gamma^{'})$ that minimizes the sum over i of

$$(\Delta P_{r,i})^2 = [P_{r,i} - (A^{'} + 10\gamma^{'} \log d_i)]^2. \tag{4.14}$$

In so doing, it implicitly stipulates that the "noise" components in the $P_{r,i}$-values have a zero sum over i. Thus, it behaves as though the form of $P_{r,i}$ is as given in the bottom line of (4.10), where the term common to all $P_{r,i}$ is $(A+Z_n)$, hereafter referred to as $A^{"}$; and the "noise" for each $P_{r,i}$-value is $(S_i - Z_n)$, hereafter referred to as $S_i^{"}$. (Note that the sum over i of $S_i^{"}$ is zero.) The application of the LSE algorithm, therefore, yields $A^{'}$ as an approximation to $A^{"}$, and the n $S_i^{'}$-values as approximations to the $S_i^{"}$-values.

The estimate for received power at point 0 is written as

$$P_{r,0}^{'} = A^{'} + 10\gamma^{'} \log d_0 + \sum_i w_i S_i^{'}. \tag{4.15}$$

In view of the above, it can also be written as

$$P_{r,0}^{'} = A^{"} + 10\gamma \log d_0 + \sum_i w_i S_i^{'} - \delta_{m,0}, \tag{4.16}$$

where, at any point k,

$$\begin{aligned} \delta_{m,k} &= \Delta A + 10\Delta\gamma \log d_k, \\ \Delta A = A" - A^{'} &\text{ and } \Delta\gamma = \gamma - \gamma^{'}. \end{aligned} \tag{4.17}$$

In Section **??** of the Appendix, we derive errors ΔA and $\Delta\gamma$.

Using these results, we can write an expression for $(P_{r,0} - P_{r,0}^{'})$ which is the dB difference at point 0 between the estimated and actual received power. The result is

$$\begin{aligned} \Delta P_{r,0} &= P_{r,0} - P_{r,0}^{'} \\ &= \left(\delta_{m,0} - \sum_{i=1}^{n} w_i \delta_{m,i}\right) + \left(S_0^{"} - \sum_{i=1}^{n} w_i S_i^{'}\right), \end{aligned} \tag{4.18}$$

where the first part reflects the total error caused by imperfect estimation of $A^{"}$ and γ, and the second part is the error due to imperfect estimation of $S_0^{"} = S_0 - Z_n$. While the formulation (4.9) has involved applying $\boldsymbol{W}$ to S-values, in actuality the path loss estimation uses $S^{"}$ (see 4.10). Unfortunately, using the same formulation for the weights in terms of the correlation matrix of $S^{"}$ can occasionally lead to problems associated with an ill-conditioned $\boldsymbol{C_n}$ matrix depending on the geometry. Thus, to cope with this, one option is to calculate $\boldsymbol{W}$ using the correlation matrix of S, as in (4.9), but apply $\boldsymbol{W}$ to $S^{"}$. This leads to very little degradation of the SM-1 results when compared with SM-0 results, as well as with results for other methods in the literature.

Further solving for $\Delta P_{r,0}$, we have,

$$\begin{aligned} \Delta P_{r,0} = S_0 &+ \sum_{i=1}^{n} S_i \left(\alpha_i \log\left(\frac{d_0}{\prod_j d_j^{w_j}}\right) - w_i\right) \\ &+ \sum_{i=1}^{n} S_i \left(\left(1 - \sum_j w_j\right)\left(\beta_i - \frac{1}{n}\right)\right); j = \{1, .., n\} \end{aligned} \tag{4.19}$$

where

$$\alpha_i = \frac{\left(\sum_{j=1}^{n} \log d_j\right) - n \log d_i}{n \sum_{j=1}^{n} (\log d_j)^2 - \left(\sum_{j=1}^{n} \log d_j\right)^2};$$
$$\beta_i = \frac{(\log d_i)\left(\sum_{j=1}^{n} \log d_j\right) - (1/n)\left(\sum_{j=1}^{n} \log d_j\right)^2}{n \sum_{j=1}^{n} (\log d_j)^2 - \left(\sum_{j=1}^{n} \log d_j\right)^2}. \tag{4.20}$$

$\Delta P_{r,0}$ is seen to be a weighted linear sum of shadow fadings S_1 through S_n at the sensors and S_0 at point 0. Therefore, $\Delta P_{r,0}$ is a zero-mean Gaussian random variable whose RMS value scales with σ.

4.3.2 The Second Method: SM-2

The obvious disadvantage of SM-1 is that the spatial correlation properties of shadow fading, and thus the weighting vector $\boldsymbol{W}$, are difficult to estimate in practice. However, the SM-1 analysis allows us to compute best-case bounds on attainable accuracy for any spatial correlation process. This provides a benchmark against which to compare less optimal but more practical schemes. Following the method of [67], where inverse distance weighting (IDW) is applied to the estimates S_i, we propose the nonparametric weighting function

$$w_i = \frac{y_{0i}^{-\nu}}{\sum_{j=1}^{n} y_{0j}^{-\nu}}; i = 1, .., n, \tag{4.21}$$

where y_{0i} is the distance from sensor i to point 0. We will use $\nu = 1$ in our calculations, as [67] shows little variation in error performance for $\nu = 1$, 2 or 3. Also note that, for any choice of ν, the n weights add to 1, as in [67], which is not necessarily true for the weights used in SM-1.

4.4 Evaluation

4.4.1 Methodology

For the sake of concreteness, we postulate a particular geometry, as shown in Fig. 4.1. In a 3-km x 3-km area, a grid of sensors are superimposed where the sensors are separated by distance $D = 640$ m. The postulated geometry is a typical coverage area that might

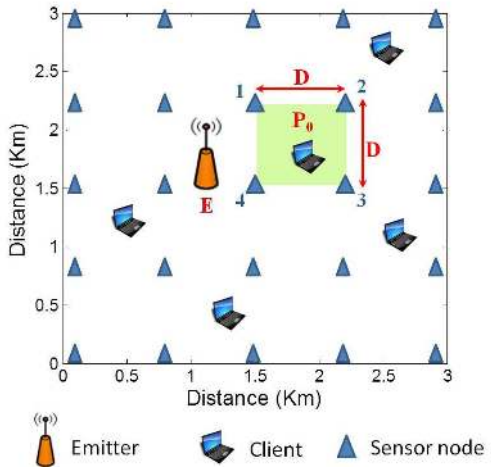

Figure 4.1: Problem geometry to be studied. The sensor layout defines a square grid, with each square having side D. Computations are made for the square shown shaded, with sensors 1, 2, 3 and 4. Interpolation methods are applied to points inside the square to estimate received power from the emitter at location E.

be used, e.g., in a cellular network with a primary emitter (base station), primary clients and secondary emitters. We will use this geometry to quantify the accuracy of specific approaches. The proposed approaches can be scaled to other dimensions and extended to other geometries[2]. Towards the objective of building a radio map, we focus on one of the sensor squares, shown by the shaded region in Fig. 4.1, and can apply our methodology to each square within the large grid. We will compute the RMS interpolation error at points inside the square by averaging over the statistical ensemble of shadow fading; we can also regard this as spatial averaging over all the squares in the grid, assuming the propagation model is statistically stationary. We assume that there is an emitter E external to this square area and all given sensors (here, $n = 4$) scans the same band, where each of the sensors measures and reports the received power from E. We assume the sensor measurements are sufficiently wideband that the effects of local multipath fading are averaged out. We continue to assume that the emitter location is known; later, however, we discuss how the case of unknown location and/or multiple emitters might be handled.

Here the impact of emitter E at any arbitrary point 0 is determined by collecting

[2]Another possibility is tessellating hexagons in place of squares, as in studies of cellular networks

Table 4.2: Simulation parameters

Parameter	**Value**
Path loss model (3GPP suggested model [73])	$15.3 + 10(3.76)\log_{10} d$ $A = 15.3, \gamma = 3.76$
Shadow fading spread	$\sigma = 5$ dB
Number of sensors	$n = 4$
Length of a side of the square	$D = 640$ m
Assumed coordinates for n sensor	$(0,0), (0,640), (640,640), (640,0)$

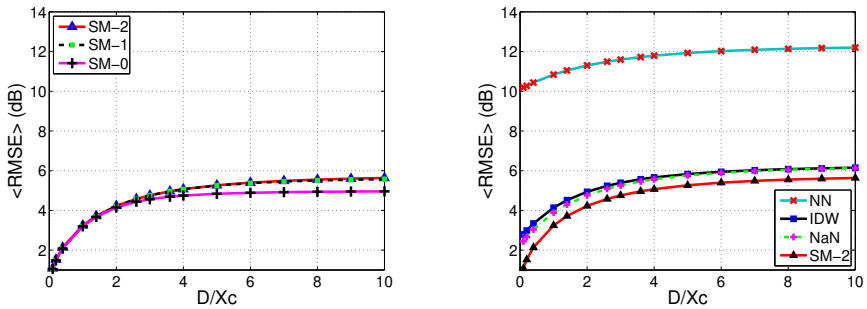

(a) Comparisons of SM-0, SM-1, SM-2

(b) Comparisons of SM-2 with Nearest Neighbor (NN), Natural Neighbor (NaN), Inverse Distance Weights (IDW)

Figure 4.2: Spatial averages over the square of RMS interpolation error, for different methods, as a function of D/X_c. Exponential correlation function, $\sigma = 5$ dB and Emitter at $E(-100, 0)$.

measurements at the $n = 4$ sensors surrounding point 0 and applying the proposed interpolation algorithms - SM-0, SM-1, and SM-2. We evaluate the performance of each algorithm with respect to RMS error as described in previous sections. Further, we provide a comparison of our proposed algorithms with several common interpolation techniques: Nearest Neighbor (NN), Inverse Distance Weighting (IDW), and Natural Neighbor (NaN). NN is the simplest interpolation technique where estimation at the point 0 is equal to the measurement at the sensor nearest to point 0. Both IDW and NaN provide estimates that are weighted sums of the n sensor measurements, with the sum of the weights being 1. For IDW, each weight is based on distance to the sensor; for NaN, the weights are based on areas, using Voronoi cells [74].

Point 0 can be anywhere inside the square, and we will find the RMS interpolation error at many such points, specifically, points on a 64×64 array distributed uniformly over the square. At every one of the $64 \times 64 = 4096$ points, we will obtain the RMS interpolation error by averaging over 10000 realizations (or instances) of

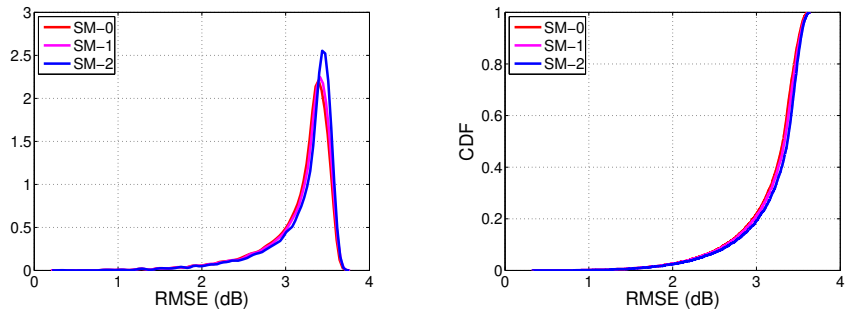

(a) Probability distribution function (b) Cumulative distribution function

Figure 4.3: Spatial distributions of RMS interpolation error over the square, for the SM family and $D/X_c = 1$. Exponential correlation function, $\sigma = 5$ dB and Emitter at $E(-100, 0)$.

$[S_0, S_1, S_2, S_3, S_4]$; and then we will average over the square. The overall spatial average will be represented by the metric $<RMSE>$,

$$< RMSE >= \sqrt{\frac{\sum_{j=1}^{m} x_j^2}{m}}, \tag{4.22}$$

where $<>$ in this case denotes a spatial average, and x_j is the RMS error at the j-th point in the 64×64 array. Other simulation parameters are listed in Table 4.2.

4.4.2 Effect of Sensor Spacing

The most important parameter of the sensor network design is the sensor density, e.g., the number of sensors per unit area. This can also be captured by the nominal spacing between sensors which, in our problem geometry, Fig. 4.1, corresponds to the side of the square, D.

Moreover, the impact of the spacing depends, not on its absolute value, but on that value relative to the distance over which shadow fading decorrelates. From (4.4) (or related correlation functions), we can use the correlation distance X_c for this purpose, and examine $<RMSE>$ as a function of D/X_c. Typically, X_c varies from several meters to a few hundred meters, depending on the type of terrain [66, 74].

Fig. 4.2 shows $<RMSE>$ as a function of D/X_c when the emitter is located at $E(-100, 0)$ with respect to given sensor coordinates (see Table 4.2). Fig. 4.2(a) compares $<RMSE>$ for proposed approaches SM-0, SM-1, and SM-2. As expected, SM-0

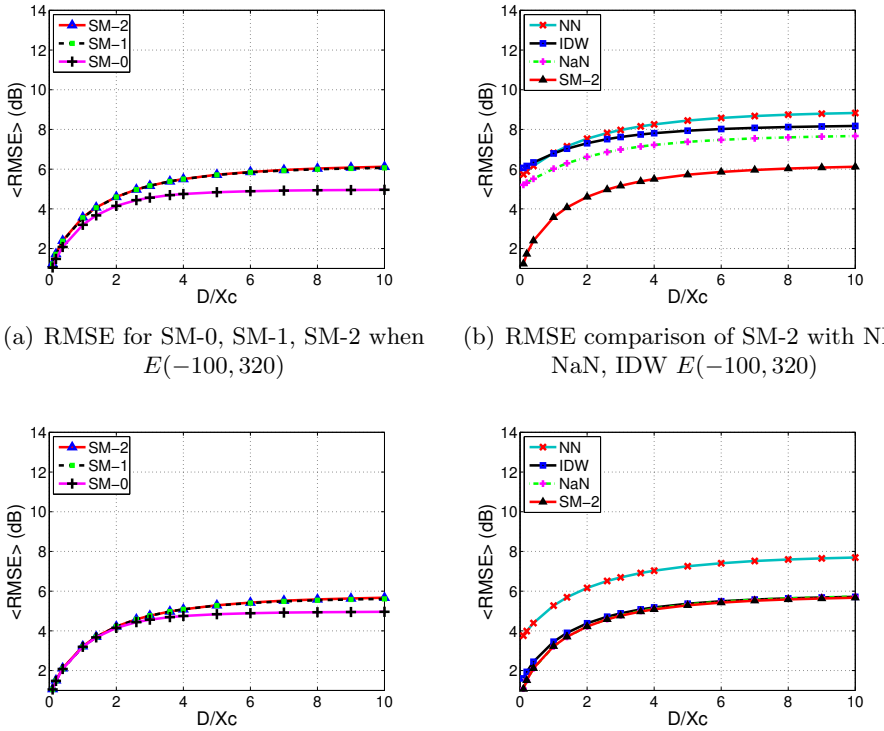

(a) RMSE for SM-0, SM-1, SM-2 when $E(-100, 320)$

(b) RMSE comparison of SM-2 with NN, NaN, IDW $E(-100, 320)$

(c) RMSE for SM-0, SM-1, SM-2 when $E(-400, -400)$

(d) RMSE comparison of SM-2 with NN, NaN, IDW $E(-400, -400)$

Figure 4.4: Effect of emitter location on $<RMSE>$ vs. D/X_c. Exponential correlation function and $\sigma = 5$ dB.

provides the lower bound of the estimation error. We note that error curves of SM-1 overlaps with SM-2, even though SM-2 lacks knowledge of the spatial correlation function. Furthermore, Fig. 4.2(b) shows that SM-2 estimates received power with the lowest RMS error when compared with the NN, IDW and NaN methods.

To affirm that $<RMSE>$ is an appropriate metric, we computed the probability density function (pdf) and its associated cumulative distribution function (CDF) over the $m = 4096$ array points within the square. Results are shown in Fig. 4.3 for the particular case $D/X_c = 1$. The major finding is the same for other values of D/X_c as well, namely, that the RMS error is fairly uniform over the square. From the figure, for example, we observe for $D/X_c = 1$ and the three SM approaches, that the RMS error is within 0.3 dB of $<RMSE>$ at 80% of the points in the array.

4.4.3 Effect of Emitter Location

For the family of SM approaches, the location of the emitter does not affect the estimate of S_0 but can affect the accuracy in estimating the median, P_m, at a given point. To demonstrate this impact, Fig. 4.4 shows plots of $<RMSE>$ vs. D/X_c for two distinct locations. For the three SM approaches, the impact of emitter location is seen to be relatively small (see 4.4(a) and 4.4(c)); comparing 4.4(b) and 4.4(d), we see that the impact on NN, NaN and IDW is greater. These trends are evident across a range of emitter locations.

4.4.4 Effect of Correlation Function

The shape of the spatial correlation function in (4.4) is exponential, but other shapes may prevail, depending on the topography. To show the robustness of RMS error results to this shape, we now consider two other cases−

Gaussian correlation function

We now consider the correlation function [75]

$$c_{ab} = \sigma^2 \exp\left[-\left(\frac{d_{ab}}{X_c}\right)^2\right] \tag{4.23}$$

Comparing Figs. 4.5(a) and 4.5(b) with Figs. 4.2(a) and 4.2(b), we see no substantial difference between the exponential and Gaussian correlation functions, (4.4) and (4.23).These functions can be considered circular, i.e., in each case, the locus of constant correlation is a circle. We next consider a correlation function that depends on direction as well as distance separation.

Elliptical correlation function

In this case, the locus of constant correlation is an ellipse, tilted at some rotation angle and having unequal major and minor axes. For one possible case, with a major-to-minor axis ratio of 3.3, we repeated the computations and obtained the results in Figs. 4.5(c)

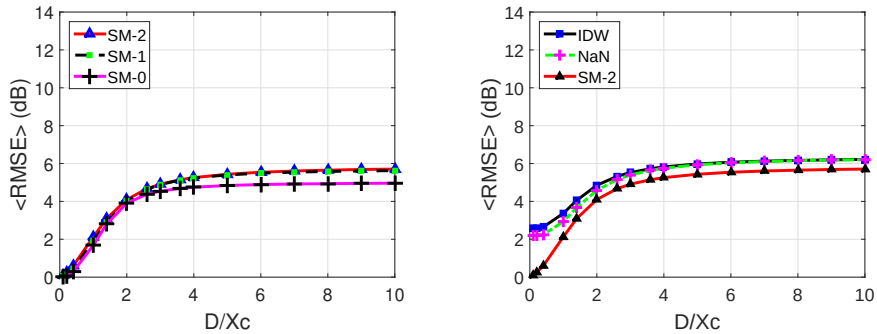

(a) RMSE for SM-0, SM-1, SM-2 for Gaussian correlation function

(b) RMSE comparison of SM-2 with NaN, IDW for Gaussian correlation function

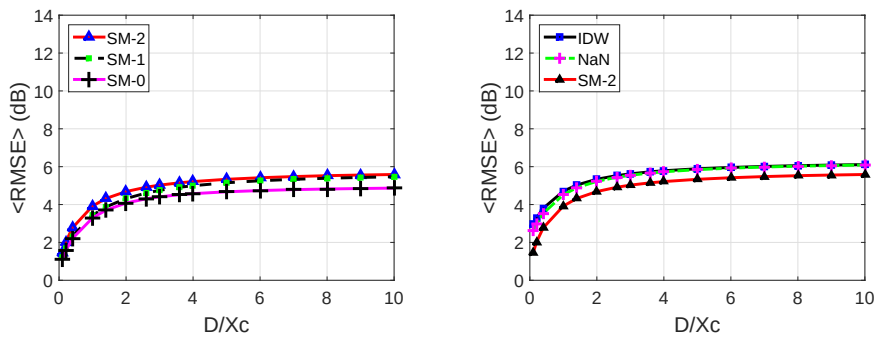

(c) RMSE for SM-0, SM-1, SM-2 for elliptical correlation function

(d) RMSE comparison of SM-2 with NaN, IDW for elliptical correlation function

Figure 4.5: Effect of spatial correlation function on $<RMSE>$ vs. D/X_c. $\sigma = 5$ dB and emitter at $E(-100, 0)$.

and 4.5(d). Again, we see no dramatic departure from results for other correlation functions.

4.5 Discussion

This section summarizes the major findings of our study through the analytical and graphical results for a square layout of sensors. We note that these findings can be generalized and scaled to other geometric configurations.

- The ideal stochastic method (SM-0) is identical to Simple Kriging and gives the lower bound on $<RMSE>$ as a function of D/X_c. The curve of $<RMSE>$ vs. D/X_c rises smoothly from (0, 0) and approaches an asymptotic value equal to σ. This error curve is independent of emitter location.

- A key attribute of SM-0, SM-1 and SM-2 is that they estimate the parameters of

the median received power, a consequence of which is that the RMS errors go to 0 as D/X_c goes to 0.

- The RMS error curves for SM-1 and SM-2 are indistinguishable from each other in all cases; thus, using the nonparametric weighting method of SM-2 incurs virtually no penalty. For large D/X_c, the errors are slightly higher than for SM-0; the gap depends on the geometry of the emitter location, but is never more than about 0.2σ (1 dB for $\sigma = 5$ dB).

- IDW is computationally simpler than NaN, but NaN yields smaller RMS errors. However, the error curves for NaN and IDW do not approach 0 as D/X_c approaches 0, in contrast to the SM cases. For both methods, the error curves are always above those for SM-2.

- The NN method is an outlier in this field of comparison. While simpler than all others, it is highly sensitive to emitter location and in some cases produces very large RMS errors compared to all others.

- SM-2 is much simpler to implement than NaN and Ideal Kriging (SM-0), and unlike the latter, requires no knowledge of the spatial correlation function. It also provides RMS errors that are fairly uniform across the coverage error.

- The behavior of the SM family of interpolation schemes is consistently better than IDW, NaN and NN for different spatial correlation functions.

Taken together, it appears that SM-2 provides the best tradeoff in terms of computational simplicity, RMSE performance, and robustness to emitter location, correlation function, and other network/environment conditions.

The construction of a radio map based on interpolation from a sparsely deployed set of distributed sensors is a promising technique for monitoring spectrum usage. The utility of such a radio map can be extended to applications such as spectrum policing, network planning and management. The currently available two weighted-sum methods, IDW and NaN, have an important 'robustness' attribute in addition to not

requiring knowledge of the spatial correlation function: They also do not require knowledge of the emitter location, or even knowledge of how many emitters are active; for each method, the operation is independent of this information. In the case of a single emitter of known location, the proposed stochastic methods (SM) can estimate path loss parameters to gain an advantage, and the result has been shown to be lower RMS errors in interpolating radio power. Notably, the practical approach SM-2 has low error in comparison with NaN and IDW when D/X_c ranges between 0 and 1 and has consistent RMS error irrespective of the emitter location. For the most part, however, either IDW or NaN can be used as backup interpolation methods whenever the single-emitter location, or number of emitters, is unknown. The opportunities suggested by this observation are worthy of further study.

Chapter 5

Coordinated Dynamic Spectrum Management of LTE and Wi-Fi Networks

In the future wireless heterogeneous network, it is reasonable to forecast that Wi-Fi and LTE will be among the dominant technologies used by RATs for access purposes. Thus, this chapter focuses on the co-channel deployment of these two technologies. LTE is designed to operate solely in a spectrum, which when operating in unlicensed spectrum, is termed LTE-U. It is suggested in 3GPP, that LTE-U will be used as a supplemental downlink, whereas the uplink will use licensed spectrum. This makes the deployment even more challenging as the UEs do not transmit in unlicensed spectrum yet experience interference from Wi-Fi transmissions. Interference scenarios in their co-channel operation are shown in Fig5.1. To alleviate these problems, we introduce a simplistic but accurate analytical model to characterize the interference between Wi-Fi and LTE networks, when they coexist and share the medium in time, frequency and space [12]. Furthermore, we have partially validated the model by performing experimental analysis in the 2.4 GHz band using USRP based LTE nodes and commercial off-the-shelf (COTS) IEEE 802.11g devices in the ORBIT testbed.

5.1 Background on Wi-Fi/LTE Co-existence

Coordination between multi-RAT networks with LTE and Wi-Fi is challenging due to the difference in the medium access control layer of the two technologies.

Wi-Fi is based on the distributed coordination function (DCF) where each transmitter senses the channel energy for transmission opportunities and collision avoidance. In particular, clear channel assessment (CCA) in Wi-Fi involves two functions to detect any on-going transmissions [76, 77] -

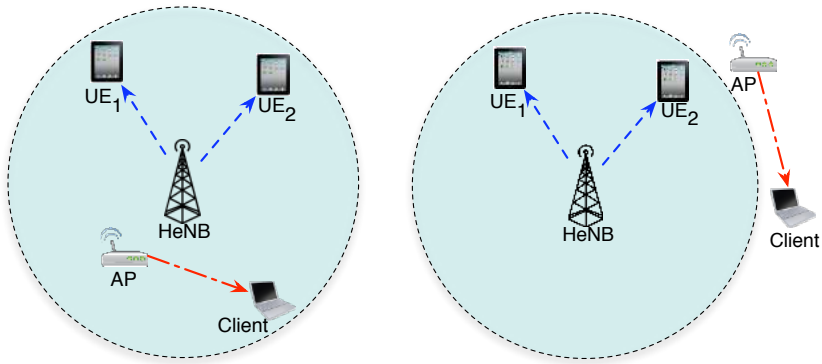

(a) Interference caused by LTE. (b) Interference caused by Wi-Fi.

Figure 5.1: Scenarios showing challenges of LTE and Wi-Fi coexistence in the same unlicensed spectrum.

1. *Carrier sense*: Defines the ability of the Wi-Fi node to detect and decode other nodes' preambles, which most likely announces an incoming transmission. In such cases, Wi-Fi nodes are said to be in the CSMA range of each other other. For the basic DCF with no RTS/CTS, the Wi-Fi throughput can be accurately characterized using the Markov chain analysis given in Bianchi's model [14], assuming a saturated traffic condition (at least 1 packet is waiting to be sent) at each node. Wi-Fi channel rates used in the [14] can be modeled as a function of Signal-to-Interference-plus-Noise ratio. Our throughput analysis given in the following sections is based on Bianchi's model.

2. *Energy detection*: Defines the ability of Wi-Fi to detect non-Wi-Fi (in this case, LTE) energy in the operating channel and back off the data transmission. If the in-band signal energy crosses a certain threshold, the channel is detected as busy (no Wi-Fi transmission) until the channel energy is below the threshold. Thus, this function becomes the key parameter for characterizing Wi-Fi throughput in the co-channel deployment with LTE.

LTE has both frequency division (FDD) and time division (TDD) multiplexing modes to operate. But to operate in unlicensed spectrum, supplemental downlink and TDD access is preferred. In either of the operations, data packets are scheduled in the

successive time frames. LTE is based on orthogonal frequency-division multiple access (OFDMA), where a subset of subcarriers can be assigned to multiple users for a certain symbol time. This gives LTE additional diversity in the time and frequency domain that Wi-Fi lacks, since Wi-Fi bandwidth is assigned to a single user at any time. Further, LTE does not assume that spectrum is shared, and consequently does not employ any sharing features in the channel access mechanisms. Thus, the coexistence performance of both Wi-Fi and LTE is largely unpredictable and may lead to unfair spectrum sharing or the starvation of one of the technologies [78, 79].

In the literature, several studies have discussed spectrum management for multi-RAT heterogeneous networks in shared frequency bands, primarily focusing on IEEE 802.11 and 802.16 networks [80–82]. Recently, Wi-Fi and LTE coexistence has been studied in the context of TV white space [83], in-device coexistence [84], and LTE-unlicensed (LTE-U) [85–87]. Several studies [86–88] propose CSMA/sensing based modifications in LTE with features like Listen-before-Talk, RTS/CTS protocol, and slotted channel access. In other studies, to enable Wi-Fi/LTE coexistence, solutions like blank LTE subframes/LTE muting (feature in LTE Release 10/11) [83, 89], carrier sensing adaptive transmission [86], interference aware power control in LTE [90] have been proposed, which require LTE to transfer its resources to Wi-Fi. These schemes give Wi-Fi transmission opportunities but also lead to performance tradeoffs for LTE. Further, time domain solutions often require time synchronization between Wi-Fi and LTE and increase channel signaling. Some aspects of frequency and LTE bandwidth diversity have been explored in studies [86] and [91], respectively. Frequency diversity is perhaps the least studied problem in Wi-Fi/LTE coexistence, while previous studies also have yet to consider dense Wi-Fi and LTE HetNet deployment scenarios in detail. Notably, in the literature, there are no previous studies experimentally evaluating the coexistence performance of Wi-Fi and LTE.

5.2 Interference Characterization

5.2.1 Interference Characterization Model

We propose an analytical model to characterize the interference between Wi-Fi and LTE, while considering the Wi-Fi sensing mechanism (clear channel assessment (CCA)) and scheduled and persistent packet transmission at LTE. To illustrate, we focus on a co-channel deployment involving a single W-iFi and a single LTE cell, which involves disseminating the interaction of both technologies in detail and establish a building block to study a complex co-channel deployment of multiple Wi-Fis/LTEs.

In a downlink deployment scenario, a single client and a full buffer (saturated traffic condition) is assumed at each AP under no MIMO. Transmit powers are denoted as $P_i, i \in \{w, l\}$ where w and l are indices to denote Wi-Fi and LTE links, respectively. We note that the maximum transmission power of an LTE small cell is comparable to that of the Wi-Fi, and thus is consistent with regulations of unlicensed bands.

The power received from a transmitter j at a receiver i is given by $P_j G_{ij}$ where $G_{ij} \geq 0$ represents a channel gain which is inversely proportional to d_{ij}^{γ} where d_{ij} is the distance between i and j and γ is the path loss exponent. G_{ij} may also include antenna gain, cable loss, wall loss, and other factors. Signal-to-Interference-plus-Noise (SINR) on the link i given as

$$S_i = \frac{P_i G_{ii}}{P_j G_{ij} + N_i}, \quad i, j \in \{w, l\}, i \neq j \tag{5.1}$$

where N_i is noise power for receiver i. Here, in the case of a single Wi-Fi and LTE, if i represents the Wi-Fi link, then j is the LTE link, and vice versa.

The throughput, $R_i, i \in \{w, l\}$, can be represented as a function of S_i as

$$R_i = \alpha_i B \log_2(1 + \beta_i S_i), \quad i \in \{w, l\}, \tag{5.2}$$

where B is a channel bandwidth; β_i is a factor associated with the modulation scheme.

[1]Throughput the paper, LTE home-eNB (HeNB) is also referred as access point (AP) for the purpose of convenience

For LTE, α_l is a bandwidth efficiency due to factors adjacent channel leakage ratio and practical filter, cyclic prefix, pilot assisted channel estimation, signaling overhead, etc. For Wi-Fi, α_w is the bandwidth efficiency of CSMA/CA, which comes from the Markov chain analysis of CSMA/CA [14] with

$$\eta_E = \frac{T_E}{\mathrm{E}[S]},\ \eta_S = \frac{T_S}{\mathrm{E}[S]},\ \eta_C = \frac{T_C}{\mathrm{E}[S]}, \tag{5.3}$$

where $\mathrm{E}[S]$ is the expected time per Wi-Fi packet transmission; T_E, T_S, T_C are the average times per $\mathrm{E}[S]$ that the channel is empty due to random backoff, or busy due to the successful transmission or packet collision (in case of multiple Wi-Fis in the CSMA range), respectively. α_w is mainly associated with η_S.

In our analysis, $\{\alpha_i, \beta_i\}$ is approximated so that - (1) for LTE, R_l matches with throughput achieved under variable channel quality index (CQI), and (2) for Wi-Fi, R_w matches throughput achieved under Biachi's CSMA/CA model.

Characterization of Wi-Fi Throughput

Assuming λ_c is CCA threshold to detect channel as busy or not, if channel energy at the Wi-Fi node is higher than λ_c, Wi-Fi would hold back the data transmission, otherwise it transmit at a data rate based on the SINR of the link. Wi-Fi throughput with and without LTE is given as

Model 1: Wi-Fi Throughput Characterization

Data: P_w: Wi-Fi Tx power; G_w: channel gain of Wi-Fi link; P_l: LTE Tx power; G_{wl}: channel gain(LTE AP, Wi-Fi UE); N_0: noise power; E_c: channel energy at the Wi-Fi (LTE interference + N_0).

Parameter: λ_C: Wi-Fi CCA threshold

Output : R_w: Wi-Fi throughput

if *No LTE* **then**

$$R_w = \alpha_w B \log_2 \left(1 + \beta_w \frac{P_w G_w}{N_0}\right).$$

else When LTE is present

if $E_c > \lambda_C$ **then**

No Wi-Fi transmission with $R_w = 0$

else

$$R_w = \alpha_w B \log_2 \left(1 + \beta_w \frac{P_w G_w}{P_l G_{wl} + N_0}\right).$$

end

end

Characterization of LTE Throughput

Due to CSMA/CA, Wi-Fi is active for an average η_S fraction of time (Eq. (5.3)). Assuming that LTE can instantaneously update its transmission rate based on the Wi-Fi interference, its throughput can be modeled as follows-

Model 2: LTE Throughput Characterization

Data: P_l: LTE Tx power; G_l: channel gain of LTE link; P_w: Wi-Fi Tx power; G_{lw}: channel gain(Wi-Fi AP,LTE UE); N_0: noise power; E_c: channel energy at Wi-Fi (LTE interference + N_0);

Parameter: λ_C: Wi-Fi CCA threshold

Output : R_l: LTE throughput

if *No Wi-Fi* **then**

$$R_{l_{\text{noW}}} = \alpha_l B \log_2 \left(1 + \beta_l \frac{P_l G_l}{N_0}\right).$$

else When Wi-Fi is present

if $E_c > \lambda_C$ **then**

No Wi-Fi transmission/interference

$$R_l = R_{l_{\text{noW}}}.$$

else

$$R_l = \alpha_l B \log_2 \left(1 + \beta_l \frac{P_l G_l}{P_l G_{lw} + N_0}\right).$$

Using (5.3) and $\eta_C = 0$ (a single Wi-Fi)

$$R_l = \eta_E R_{l_{\text{noW}}} + \eta_S R_l$$

end

end

5.2.2 Experimental Validation

In this section, we experimentally validate proposed interference characterization models using experiments involving the ORBIT testbed and USRP radio platforms available at WINLAB [92, 93]. An 802.11g Wi-Fi link is set up using Atheros AR928X wireless network adapters [94] and an AP implementation with *hostapd* [95]. For LTE, we use *OpenAirInterface*, an open-source software implementation, which is fully compliant

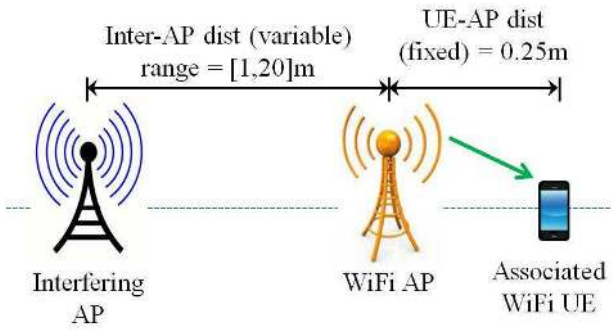

Figure 5.2: Experimental scenario to evaluate the throughput performance of Wi-Fi w_1 in the presence of interference (LTE/other Wi-Fi/white noise) when both w_1 and interference operated on the same channel in 2.4 GHz

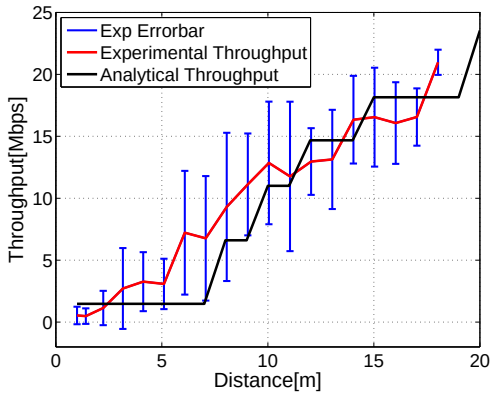

Figure 5.3: Comparative results analytical model and experiments to show the effect of LTE on the throughput of Wi-Fi 802.11g when distance between LTE eNB and Wi-Fi link is varied.

with 3GPP LTE standard (release 8.6) and set in transmission mode 1 (SISO) [96]. Currently, *OpenAirInterface* is in the development mode for USRP based platforms with limited working LTE operation parameters.

In our experiment, depicted as the scenario shown in figure 5.2, we study the effect of interference on the Wi-Fi link w_1. For link w_1, the distance between the AP and client is fixed at 0.25 m (very close so that the maximum throughput is guaranteed when interference is present. Experimentally, we observe maximum throughput as 22.2 Mbps). The distance between the interfering AP and Wi-Fi AP is varied in the range of 1 to 20 m. The throughput of w_1 is evaluated under three sources of interference - LTE and Wi-Fi, when both w_1 and the interference AP is operated on the same channel

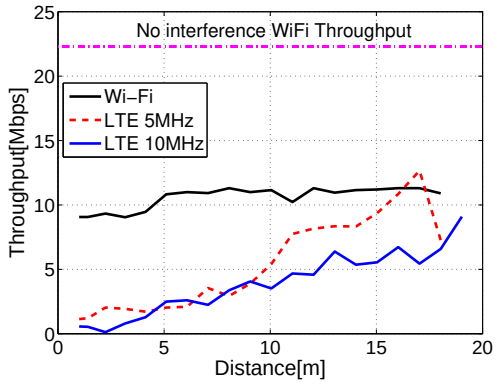

Figure 5.4: Comparative results analytical model and experiments to show the effect of LTE on the throughput of Wi-Fi 802.11g when distance between LTE HeNB (AP) and Wi-Fi link is varied.

in the 2.4 GHz spectrum band. These experiments are carried in the 20 m-by-20 m ORBIT room in WINLAB, which has an indoor Line-of-Sight (LoS) environment. For each source of interference, Wi-Fi throughput is averaged over 15 sets of experiments with variable source locations and trajectories between interference and w_1.

In the first experiment, we perform a comparison study to evaluate the effect of LTE interference on w_1, observed by experiments and computed by interference characterization model. In this case, LTE signal is lightly loaded on 5 MHz of bandwidth mainly consist of control signals. Thus, the impact of such LTE signal over the Wi-Fi band is equivalent to the low power LTE transmission. Thus, we incorporate these LTE parameters in our analytical model. As shown in figure 5.3, we observe that both experimental and analytical values match the trend very closely, though with some discrepancies. These discrepancies are mainly due to the fixed indoor experiment environment and lack of a large number of experimental data sets. Additionally, we note that even with the LTE control signal (without any scheduled LTE data transmission), performance of Wi-Fi gets impacted drastically.

In the next set of experiments, we study the throughput of a single Wi-Fi link in the presence of different sources of interference - (1) Wi-Fi, (2) LTE operating at 5 MHz, and (3) LTE operating at 10 MHz, evaluating each case individually. For this part, full-band occupied LTE is considered with the maximum power transmission of

Table 5.1: Network parameters of Wi-Fi/LTE deployment

Parameter	**Value**	**Parameter**	**Value**
Scenario	Downlink	Tx power	20 dBm
Spectrum band	2.4 GHz	Channel bandwidth	20 MHz
Traffic model	Full buffer via saturated UDP flows		
AP antenna height	10 m	User antenna height	1 m
Path loss model	$36.7\log_{10}$(d[m]) + 22.7 + $26\log_{10}$(frq [GHz])		
Noise Floor	-101 dBm, (-174 cBm thermal noise/Hz)		
Channel	No shadow/Rayleigh fading		
Wi-Fi	802.11n: SISO		
LTE	FDD, Tx mode-1 (SISO)		

100 mW. As shown in figure 5.4, when the Wi-Fi link operates in the presence of other Wi-Fi links, they share channel according to the CSMA/CA protocol and throughput is reduced approximately by half. In the both the cases of LTE operating at 5 and 10 MHz, due to lack of coordination, Wi-Fi throughput gets impacted by maximum upto 90% compared to no interference Wi-Fi throughput and $20 - 80\%$ compared to Wi-Fi thorughput in the presence of other Wi-Fi link. These results indicate significant inter-system interference in the baseline case without any coordination between systems.

5.2.3 Motivational Example

We extend our interference model to complex scenarios involving co-channel deployment of a single link Wi-Fi and LTE for the detailed performance evaluation. As shown in figure 5.5, UE_i, associated AP_i and interfering AP_j, $i, j \in \{w, l\}, i \neq j$, are deployed in a horizontal alignment. The distance, d_A, between UE_i and AP_i is varied between 0 and 100 m. At each value of d_A, the distance between UE_i and AP_j is varied in the range of -100 to 100 m. Assuming UE_i is located at the origin $(0, 0)$, if AP_j is located on the negative X-axis then the distance is denoted as $-d_I$, otherwise as $+d_I$, where d_I is an Euclidean norm $\|\text{UE}_i, \text{AP}_j\|$. In the shared band operation of Wi-Fi and LTE, due to the CCA sensing mechanism at the Wi-Fi node, the distance between Wi-Fi and LTE APs (under no shadow fading effect in this study) decides the transmission or shutting off of Wi-Fi. Thus, the above distance convention is adopted to embed the effect of distance between AP_i and AP_j. Simulation parameters for this set of simulations are

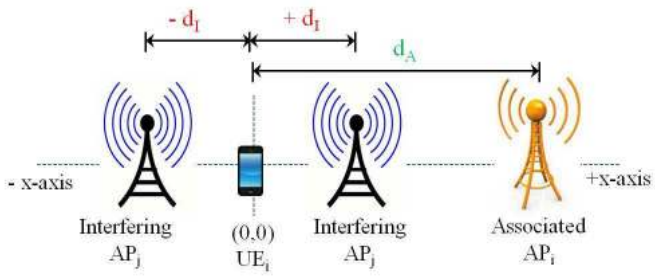

Figure 5.5: Experimental scenario to evaluate the throughput performance of Wi-Fi w_1 in the presence of interference (LTE/other Wi-Fi/white noise) when both w_1 and interference operated on the same channel in 2.4 GHz

given in Table 5.1.

Figure 5.6 shows the Wi-Fi performance in the presence of LTE interference. As shown in figure 5.6(a), the Wi-Fi throughput is drastically deteriorated in the co-channel LTE operation, leading to zero throughput for 80% of the cases and an average 91% of throughput degradation compared to standalone operation of Wi-Fi. Such degradation is explained by figure 5.6(b). Region *CCA_busy* shows the shutting off of the Wi-Fi AP due to the CCA mechanism, where high energy is sensed in the Wi-Fi band. This region corresponds to cases when Wi-Fi and LTE APs are within $\sim$ 20m of each other. In the *low SINR* region, the Wi-Fi link does not satisfy the minimum SINR requirement for data transmission, thus the Wi-Fi throughput is zero. *High SINR* depicts the data transmission region that satisfies SINR and CCA requirements and throughput is varied based on variable data rate/SINR.

On the other hand, figure 5.7 depicts the LTE throughput in the presence of Wi-Fi interference. LTE throughput is observed to be zero in the *low SINR* regions, which is 45% of the overall area and the average throughput degradation is 65% compared to the standalone LTE operation. Under identical network parameters, overall performance degradation for LTE is much lower compared to that of Wi-Fi in the previous example. The reasoning for such a behavior discrepancy is explained with respect to figure 5.7(b) and the Wi-Fi CCA mechanism. In the *CCA_busy* region, Wi-Fi operation is shut off and LTE operates as if no Wi-Fi is present. In both LTE and the previous Wi-Fi examples, *low SINR* represents the hidden node problem where two APs do not detect

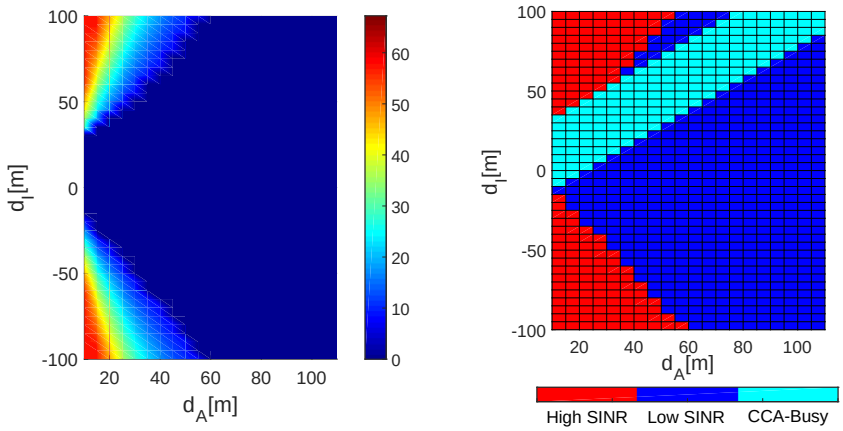

(a) A heat map of Wi-Fi throughput (Mbps)

(b) Wi-Fi performance sections- High SINR: non-zero throughput, Low SINR: SINR below minimum SINR requirement, CCA_busy: shutting off of Wi-Fi due to channel is sensed as busy

Figure 5.6: Wi-Fi performance as a function of distance(Wi-Fi AP, associated Wi-Fi UE) d_A and distance(Interfering LTE AP, Wi-Fi UE) d_I

each other's presence and data transmission at an UE suffers greatly.

5.3 System Model

As seen in the previous section, when two (or more) APs of different Wi-Fi and LTE networks are deployed in the same spectrum band, APs can cause severe interference to one another. In order to alleviate inter-network interference, we propose joint coordination based on (1) power, and (2) time division channel access optimization. We assume that both LTE and Wi-Fi share a single spectrum channel and operate on the same amount of bandwidth. We also note that clients associated to one AP cannot join other Wi-Fi or LTE APs. This is a typical scenario when multiple autonomous operators deploy APs in the shared band. With the help of the proposed SDN architecture, power level and time division channel access parameters are forwarded to each network based on the throughput requirement at each UE. To the best of our knowledge, such an optimization framework has not yet received much attention for the coordination between Wi-Fi and LTE networks.

We consider a system with N Wi-Fi and M LTE networks. W and L denote the

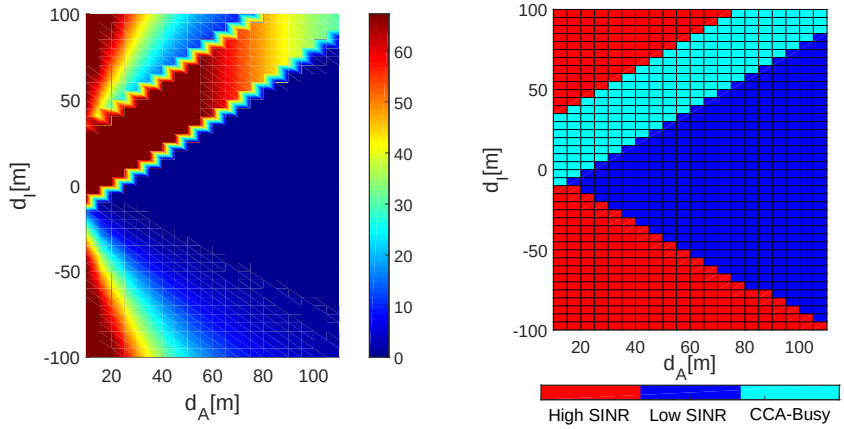

(a) A heat map of LTE throughput (Mbps)

(b) LTE performance sections- High SINR: non-zero throughput, Low SINR: SINR below minimum SINR requirement, CCA_busy: shutting off of Wi-Fi due to channel is sensed as busy

Figure 5.7: LTE performance as a function of distance(LTE AP, associated LTE UE) d_A and distance(Interfering Wi-Fi AP, LTE UE) d_I

sets of Wi-Fi and LTE links, respectively. We maintain all assumptions, definitions and notations as described in Section 5.2.1. For notational simplicity, we redefine $R^i = \alpha^i B \log_2(1 + \beta^i S_i)$ as $R^i = \alpha^i \log_2(1 + \beta^i S_i)$, where constant parameter B is absorbed with α^i. Additional notation are summarized in Table 5.2.

In order to account for the co-channel deployment of multiple Wi-Fi networks, we assume that time is shared equally when multiple Wi-Fi APs are within CSMA range due to the Wi-Fi MAC layer. We denote the set of Wi-Fi APs within the CSMA range of $\text{AP}_i, \forall i$ as M_i^a and those outside of carrier sense but within interference range as M_i^b. When AP_i shares the channel with $|M_i^a|$ other APs, its share of the channel access time get reduced to approximately $1/(1 + |M_i^a|)$. Furthermore, M_i^b signifies a set of potential hidden nodes for $\text{AP}_i, \forall i$. To capture the effect of hidden node interference from APs in the interference range, parameter ζ is introduced which lowers the channel access time and thus, the throughput. Average reduction in channel access time at AP_i is $1/(1 + \zeta|M_i^b|)$ where ζ falls in the range $[0.2, 0.6]$ [15]. Therefore, the effective Wi-Fi throughput can be written as

Table 5.2: Definition of notations

Notation	**Definition**
w, l	indices for Wi-Fi and LTE network, respectively
W	the set of Wi-Fi links
L	the set of LTE links
P_j^i	Transmission power of j-th AP of $i, \in \{w, l\}$
G_{ij}	Channel gain between nodes i and j
R_j^i	Throughput at j-th link of $i, \in \{w, l\}$
S_j^i	SINR at j-th link of $i, \in \{w, l\}$
B	Channel Bandwidth
N_0	Noise level
α^i, β^i	Efficiency parameters of network $i \in \{w, l\}$
M_i^a	Set of Wi-Fi APs in the CSMA range of AP i
M_i^b	Set of Wi-Fi APs in the interference range of AP i
ζ	Hidden node interference parameter
η	Fraction of channel access time for network $i, i \in \{w, l\}$ when $j, j \in \{w, l\}, j \neq i$, access channel for $1 - \eta$ fraction of time

$$R_i^w = a_i b_i \alpha^w \log_2(1 + \beta^w S_i^w), \quad i \in W, \\ \text{with } a_i = \frac{1}{1 + |M_i^a|} \text{ and } b_i = \frac{1}{1 + \zeta |M_i^b|}. \tag{5.4}$$

SINR of Wi-Fi link, $i, \forall i$, in the presence of LTE and no LTE is described as

$$S_i^w = \begin{cases} \dfrac{P_i^w G_{ii}}{N_0}, & \text{if no LTE;} \\ \dfrac{P_i^w G_{ii}}{\sum_{j \in L} P_j^l G_{ij} + N_0}, & \text{if LTE,} \end{cases} \tag{5.5}$$

where the term $\sum_{j \in L} P_j^l G_{ij}$ is the interference from all LTE networks at a Wi-Fi link i.

The throughput definition of the LTE link $i, \forall i$ remains the same as in Section 5.2.1:

$$R_i^l = \alpha^l \log_2(1 + \beta^l S_i).$$

The SINR of the LTE link, $i, \forall i$, in the presence of Wi-Fi and no Wi-Fi is described as

$$S_i^l = \begin{cases} \dfrac{P_i^l G_{ii}}{\sum_{j \in L, j \neq i} P_j^l G_{ij} + N_0}, \text{ if no Wi-Fi;} \\ \dfrac{P_i^l G_{ii}}{\sum_{j \in L, j \neq i} P_j^l G_{ij} + \sum_{k \in W} a_k P_k^w G_{ik} + N_0}, \text{ if Wi-Fi,} \end{cases} \tag{5.6}$$

where terms $\sum_{j \in L, j \neq i} P_j^l G_{ij}$ and $\sum_{k \in W} a_k P_k^w G_{ik}$ signifies the interference contribution from other LTE links and Wi-Fi links. For the k-th Wi-Fi link, $\forall k$, the interference is reduced by a factor a_k to capture the fact that the k-th Wi-Fi is active approximately for only a_k fraction of time due to the CSMA/CA protocol at Wi-Fi.

For a given model, inter-network coordination is employed to assure a minimum throughput requirement, thus the guaranteed availability of the requested service at each UE. For this purpose, we have implemented our optimization in two stages as described in following subsections.

5.4 Coordination via Joint Optimization

5.4.1 Joint Power Control Optimization

Here, the objective is to optimize the set of transmission power $P_i, i \in \{\mathcal{W}, \mathcal{L}\}$ at Wi-Fi and LTE APs, which maximizes the aggregated Wi-Fi+LTE throughput. Conventionally, LTE supports the power control in the cellular network. By default, commercially available Wi-Fi APs/routers are set to maximum level [97]. But adaptive power selection capability is incorporated in available 802.11a/g/n Wi-Fi drivers, even though it is not invoked very often. Under the SDN architecture, transmission power level can be made programmable to control the influence of interference from any AP at neighboring radio devices based on the spectrum parameters [98].

For the maximization of aggregated throughput, we propose a geometric programming (GP) based power control [99]. For the problem formulation, throughput, given by Eq. 5.2, can approximated as

$$R_i = \alpha_i \log_2(\beta_i S_i), \quad i \in \{\mathcal{W}, \mathcal{L}\}. \tag{5.7}$$

This equation is valid when $\beta_i S_i$ is much higher than 1. In our case, this approximation is reasonable considering minimum SINR requirements for data transmission at both Wi-Fi and LTE. The aggregate throughput of the WiFi+LTE network is

$$\begin{aligned}\mathbb{R} &= \sum_{i\in\mathcal{W}} a_i b_i \alpha_w \log_2(\beta_w S_i) + \sum_{j\in\mathcal{L}} \alpha_l \log_2(\beta_l S_j) \\ &= \log_2\left[\left(\prod_{i\in\mathcal{W}} (\beta_w S_i)^{a_i b_i \alpha_w}\right)\left(\prod_{j\in\mathcal{L}} (\beta_l S_i)^{\alpha_l}\right)\right].\end{aligned} \tag{5.8}$$

In the coordinated framework, it is assumed that Wi-Fi parameters a_i and b_i are updated periodically. Thus, these are considered as constant parameters in the formulation. Also, $\alpha_i, \beta_i, i \in \{w, l\}$ are constant in the network. Therefore, aggregate throughput maximization is equivalent to maximization of a product of SINR at both Wi-Fi and LTE links. Power control optimization formulation is given by:

$$\begin{aligned}\text{maximize} \quad & \left(\prod_{i\in\mathcal{W}} (\beta_w S_i)^{a_i b_i \alpha_w}\right)\left(\prod_{j\in\mathcal{L}} (\beta_l S_i)^{\alpha_l}\right) \\ \text{subject to} \quad & R_i \geq R_{i,\min}, \quad i \in \mathcal{W}, \\ & R_i \geq R_{i,\min}, \quad i \in \mathcal{L}, \\ & \sum_{k\in M_i^b} P_k G_{ik} + \sum_{j\in\mathcal{L}} P_j G_{ij} + N_0 < \lambda_c, \ i \in W, \\ & 0 < P_i \leq P_{\max}, \quad i \in \mathcal{W}, \\ & 0 < P_i \leq P_{\max}, \quad i \in \mathcal{L}.\end{aligned} \tag{5.9}$$

Here, the first and second constraints are equivalent to $S_i \geq S_{i,min}, \forall i$ which ensures that SINR at each link achieves a minimum SINR requirement, thus leading to non-zero throughput at the UE. The third constraint assures that channel energy at a WiFi (LTE interference + interference from Wi-Fis in the interference zone + noise power) is below the clear channel assessment threshold λ_c, thus Wi-Fi is not shut off. The fourth and fifth constraints follow the transmission power limits at each link. Unlike past power control optimization formulations for cellular networks, Wi-Fi-LTE coexistence involves meeting the SINR requirement at a Wi-Fi UE and, additionally, the CCA threshold at

a Wi-Fi AP.

For multiple Wi-Fi and LTE links, to ensure the feasibility of the problem where all constrains are not satisfied, notably for Wi-Fi links, we relax the minimum data requirement constraint for LTE links. In our case, we reduce the minimum data requirement to zero. This is equivalent to shutting off certain LTE links which cause undue interference to neighboring Wi-Fi devices.

5.4.2 Joint Time Division Channel Access Optimization

The relaxation of minimum throughput constraint in the joint power control optimization leads to throughput deprivation at some LTE links. Thus, joint power control is not sufficient when system demands to have non-zero throughput at each UE. In such cases, we propose a time division channel access optimization framework where network of each RAT take turns to access the channel. Assuming network $i, i \in \{w, l\}$ access the channel for $\eta, eta \in [0, 1]$, fraction of time, network $j, j \in \{w, l\}, j \neq i$, holds back the transmission and thus no interference occurs at i from j. For remaining $1 - \eta$ fraction of time, j access the channel without any interference from i. This proposed approach can be seen as a subset of power assignment problem, where power levels at APs of network $i, i \in \{w, l\}$, is set to zero in their respective time slots. The implementation of the protocol is out of scope of this paper.

In this approach, our objective is to optimize η, the time division of channel access, such that it maximizes the minimum throughput across both Wi-Fi and LTE networks. We propose the optimization in two steps -

Power control optimization across network of same RAT

Based on the GP-formulation, the transmission power of the APs across the same network $i, i \in \{w, l\}$, is optimized for Wi-Fi and LTE, respectively, as

$$\begin{aligned} \text{maximize} \quad & \sum_{i \in \mathcal{W}} R_i \\ \text{subject to} \quad & R_i \geq R_{i,\min}, \;\; i \in \mathcal{W} \\ & 0 \leq P_i \leq P_{\max}, \;\; i \in \mathcal{W}, \\ & \sum_{k \in M_i^b} P_k G_{ik} + N_0 < \lambda_c, \; i \in \mathcal{W}. \end{aligned} \tag{5.10}$$

and

$$\begin{aligned} \text{maximize} \quad & \sum_{i \in \mathcal{L}} R_i \\ \text{subject to} \quad & R_i \geq R_{i,\min}, \;\; i \in \mathcal{L} \\ & 0 \leq P_i \leq P_{\max}, \;\; i \in \mathcal{L}. \end{aligned} \tag{5.11}$$

Here, the objective function is equivalent to maximizing the product of SINRs at the networks $i, i \in \{w, l\}$. The first and second constraints ensure that we meet the minimum SINR and transmission power limits requirements at all links of i. In this formulation, SINR at Wi-Fi and LTE respectively given as

$$\begin{aligned} S_i =& \frac{P_i G_{ii}}{N_0}, \;\; i \in \mathcal{W}, \\ S_i =& \frac{P_i G_{ii}}{\sum_{j \in \mathcal{L}, j \neq i} P_j G_{ij} + N_0}, \;\; i \in \mathcal{L}. \end{aligned}$$

which are first cases in equations (5.5) and (5.6), respectively.

Joint time division channel access optimization

This is the joint optimization across both Wi-Fi and LTE networks which is formulated using max-min fairness optimization as given below

$$\begin{aligned} \text{maximize} \quad & \min\left(\eta R_{i \in \mathcal{W}}, (1-\eta) R_{j \in \mathcal{L}}\right) \\ \text{subject to} \quad & 0 \leq \eta \leq 1. \end{aligned} \tag{5.12}$$

Here, throughput values at all Wi-Fi and LTE nodes are considered as a constant, which is the output of the previous step. The Time division channel access parameter η is optimized so that it maximizes the minimum throughput across all UEs.

5.5 Evaluation of Joint Coordination

5.5.1 Single Link Co-channel Deployment

We begin with the motivational example of co-channel deployment of one Wi-Fi and one LTE links, as described in § 5.2.3. Fig. 5.8 shows the heatmap of improved throughput of Wi-Fi link, when joint Wi-Fi and LTE coordination is provided in comparison with the throughput with no coordination as shown in Fig. 5.6 . Similarly, Fig. 5.9 shows the heatmap of improved throughput of LTE link, when joint coordination is provided in comparison with the throughput with no coordination, as shown in Fig. 5.7.

For both the figures 5.8 and 5.9, in their respective scenarios, though joint power control improves the overall throughput for most of topological scenarios (see Fig. (a) of 5.8 and 5.9), it is not an adequate solution for topological combination marked by *infeasible* region as given in Fig. (b) of 5.8 and 5.9. The infeasible region signifies the failure to attain the CCA threshold at Wi-Fi AP and link SINR requirement when the UE and interfering AP are very close to each other. When we apply time division channel access optimization for a given scenario, we do not observe any infeasible region, in fact optimization achieves almost equal and fair throughput at both Wi-Fi and LTE links, as shown in Fig. (c) of 5.8 and 5.9. On the downside, this optimization does not consider cases when Wi-Fi and LTE links can operate simultaneously without causing severe interference to each other. In such cases, throughput at both Wi-Fi and LTE is degraded.

Fig. 5.10 summarizes the performance of Wi-Fi and LTE links in terms of 10th percentile and mean throughput. We note that the 10th percentile throughput of both Wi-Fi and LTE is increased to $15 - 20$ Mbps for time division coordination compared to $\sim$ zero throughput for no and power coordination. We observe 200% and 350% Wi-Fi mean throughput gains due to power and time division channel access, respectively,

compared to no coordination. For LTE, throughput gains for both of these coordination is $\sim 25 - 30\%$. It appears that time division channel access coordination does not offer any additional advantage to LTE in comparison with power coordination. But it brings the throughput fairness between Wi-Fi and LTE which is required for the co-existence in the shared band.

5.5.2 Multiple Links Co-channel Deployment

Multiple overlapping Wi-Fi and LTE links are randomly deployed in 200-by-200 sq. meter area which depicts the typical deployment in residential or urban hotspot. The number of APs of each Wi-Fi and LTE networks are varied between 2 to 10 where number of Wi-Fi and LTE links are assumed to be equal. For the simplicity purpose, we assume that only single client is connected at each AP and their association is predefined. The given formulation can be extended for multiple client scenarios. In the simulations, the carrier sense and interference range for Wi-Fi devices are set to 150 meters and 210 meters, respectively. The hidden node interference parameter is set to 0.25.

Figures 5.11(a) and 5.11(a) show the percentile and mean throughput values of Wi-Fi and LTE links, respectively, for when number of links for each Wi-Fi and LTE networks is set at $N = \{2, 5, 10\}$. The throughput performance is averaged over 10 different deployment topologies of Wi-Fi and LTE links. From Fig. 5.11(a), it is clear that 10 percentile Wi-Fi UEs get throughput starved due to LTE interference with no coordination. This is consistent with results from single link simulations. With coordination, both joint power control and time division channel access, we achieve a large improvement in the 10th percentile throughput. Joint power control improves mean Wi-Fi throughput by 15-20% for all N. On the other hand, time division channel access achieves throughput gain (40-60%) only at higher values of $N = \{5, 10\}$.

Throughput performance of LTE, on the other hand, deteriorates in the presence of coordination compared to when no coordination is provided. This comes from the fact that, in case of no coordination, LTE causes undue impact at Wi-Fi nodes causing them to hold off data transmission, while LTE experiences no Wi-Fi interference. Joint

coordination between Wi-Fi and LTE networks brings the notion of fairness in the system and allocates spectrum resources to otherwise degraded Wi-Fi links. In the joint power control optimization, though certain LTE links (maximum 1 link for $N = 10$) have to be dropped from network with zero throughput, but overall mean throughput is typically 150 to 400% greater than Wi-Fi throughput.

We observe that for small numbers of Wi-Fi links, joint time division channel access degrades the performance of both Wi-Fi and LTE. But as the number of links grows, coordinated optimization results in allocation of orthogonal resources (e.g. separate channels) giving greater benefit than full sharing of the same spectrum space, as is the case for power control optimization.

This study investigates inter-system interference in shared spectrum scenarios with both Wi-Fi and LTE operating in the same band. An analytical model has been developed for evaluation of the performance and the model has been partially verified with experimental data. The results show that significant performance degradation results from uncoordinated operation of Wi-Fi and LTE in the same band. To address this problem, we further presented an architecture for coordination between heterogeneous networks, with a specific focus on LTE-U and Wi-Fi, to cooperate and coexist in the same area. This framework is used to exchange information between the two networks for a logically centralized optimization approach that improves the aggregate throughput of the network. Our results show that, with joint power control and time division multiplexing, the aggregate throughput of each of the networks becomes comparable, thus realizing fair access to the spectrum. In future work, we plan to extend our analytical model and optimization framework to study realistic user applications for which full buffer traffic conditions cannot be assumed. We further plan to extend the optimization framework to exploit the frequency diversity for joint coordination of Wi-Fi and LTE.

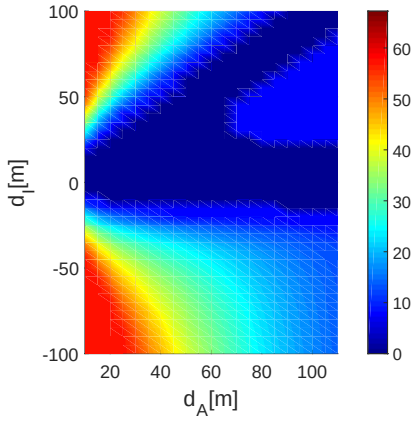

(a) A heat map of Wi-Fi throughput when joint power Coordination (Mbps)

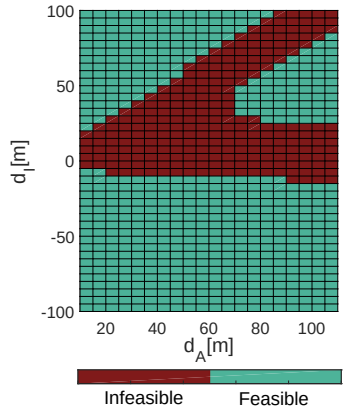

(b) Feasibility region of joint power Coordination

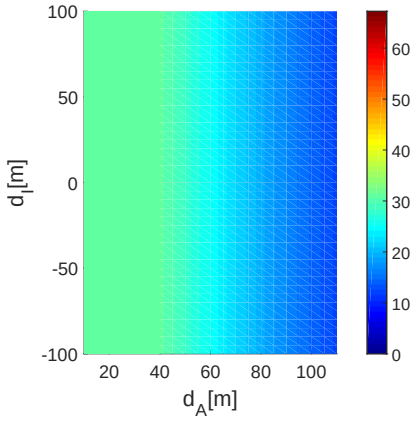

(c) A heat map of Wi-Fi throughput when time division channel access coordination (Mbps)

Figure 5.8: Wi-Fi performance under joint Wi-Fi and LTE coordination (d_A: dist(Wi-Fi AP, associated UE), d_I: dist(Interfering LTE AP, Wi-Fi UE))

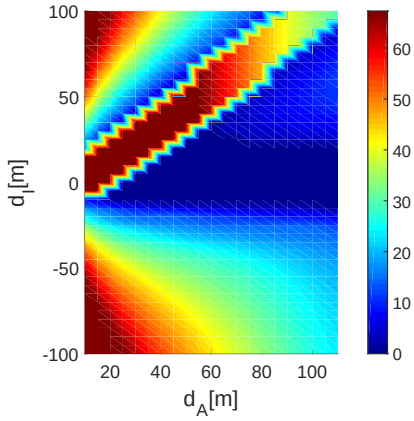

(a) A heat map of LTE throughput when joint power Coordination (Mbps)

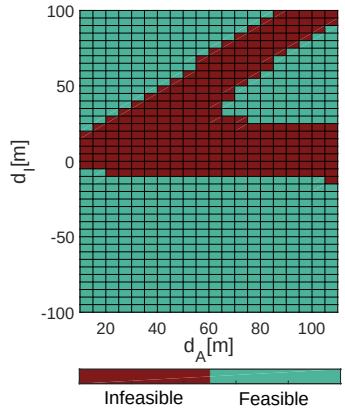

(b) Feasibility region of joint power Coordination

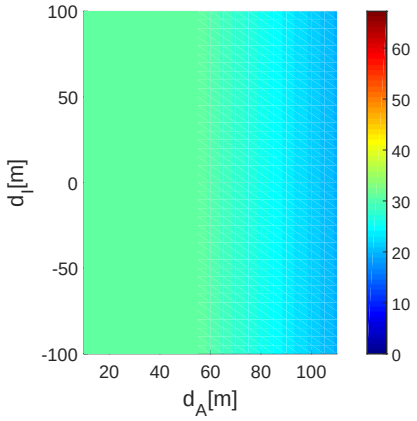

(c) A heat map of LTE throughput when time division channel access coordination (Mbps)

Figure 5.9: LTE performance under joint Wi-Fi and LTE coordination (d_A: dist(LTE AP, associated UE), d_I: dist(Interfering Wi-Fi AP, LTE UE))

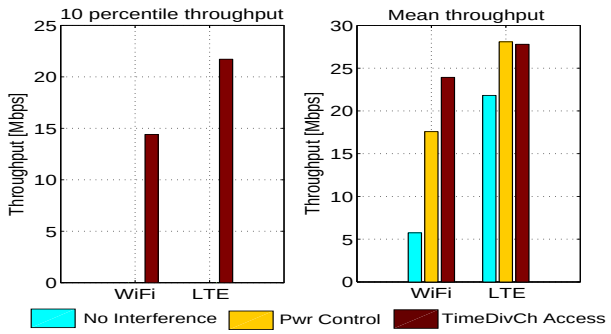

Figure 5.10: 10 percentile and mean LTE throughput for a single link Wi-Fi and LTE co-channel deployment

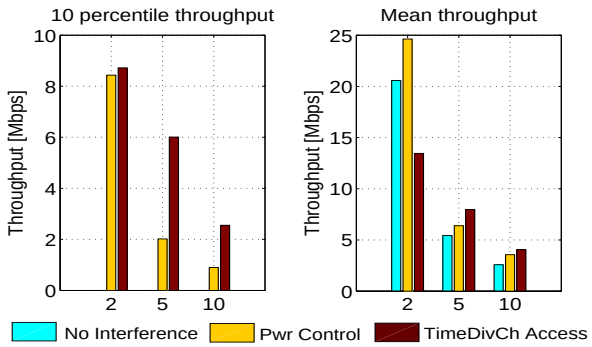

(a) 10 percentile and mean Wi-Fi throughput for $N = \{2, 5, 10\}$

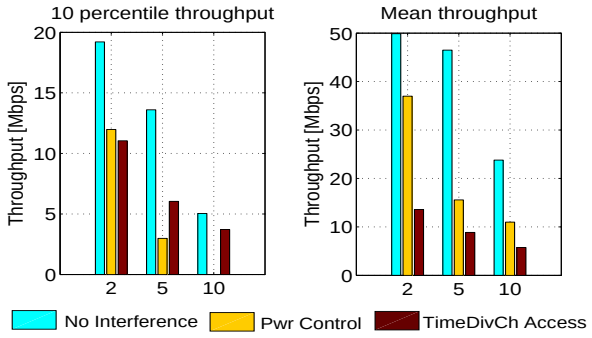

(b) 10 percentile and mean LTE throughput for $N = \{2, 5, 10\}$

Figure 5.11: Multi-link throughput performance under power control and time devision channel access optimization. N = no. of LTE links = no. of Wi-Fi links.

Chapter 6

Conclusion

In summary, the objective of the thesis is to support dynamic spectrum management to coordinate multiple operators and radio access technologies (RATs) network and develop underlying models and algorithms for coexistence characterization, spectrum usage and network coordination for high density small cell deployment.

We begun with exploring the challenge of using mobile wireless LAN hotspots to provide cellular-to-Wi-Fi tethering when there is a background fabric of fixed wireless networks that could potentially introduce interference degradation. By examining the specific case of a mobile Wi-Fi hotspot deployed next to a dense collection of fixed Wi-Fi networks, we observed large degradation in throughput at mobile hotspot because of dynamic change in interference pattern around the hotspot due to its mobility. Its throughput is improved with the application of proposed adaptive channel assignment mechanism along with a consideration of its mobility speed. The results of our investigation served as valuable lessons that can be extrapolated to exist in the more general scenario involving multiple RATs and multiple operators in which undue interference arises because of the lack of coordination between different wireless systems. This justified the need for improvements in the management and coordination for distributively deployed wireless systems. In order for such new spectrum coordination architectures to be successful, they must utilize a toolbox of algorithms and models that can appropriately inform the various decision making processes associated with coordination, and thus later parts of the thesis were focused on developing tools that support decision processes associated spectrum coordination.

Next, while investigating radio channel simulator toolbox, we studied a wireless channel where each multipath response can be described by a set of mean-squared

amplitude components and relative delays. Moreover, the number of taps needed to characterize any link depends on the product of bandwidth W and RMS delay spread τ_{rms} of the channel. To capture the behavior of all possible links of multi-nodes network can become prohibitive to implement when the underlying communication bandwidth is of several hundred MHz. Thus, in an effort to reduce hardware emulation complexity, we factored and proposed channel modeling for two cases: (1) emulation of source-to-receiver channel with 3-tap channel approximation which matches the power delay profile (PDP) of the 'true' channel, (2) emulation of pairwise interference between nodes where the required number of taps for each interference link is derived to be $2W\tau_{rms}$ while maintaining the cumulative distribution function (CDF) of total interference power, taken over the fading. Our results show that loss in accuracy due to these approximation methods is significantly low. We further show that we achieve the improvement of 50% in reduction in required taps. For large values of $W\tau_{rms}$, these approximations lead to even more reduction in number of taps and, thus, further limit the cost and complexity of hardware emulators. Our analysis is made for the case of an exponential PDP on each link. Further work can test the approach for other PDP shapes, e.g., channels with sparse multipath, and for unequal conditions (PDP and average power) among the links.

In the next part, we explored the challenge of creating a database of geographical radio maps which could serve as a building block to applications such as spectrum policing, network planning and management. We observed that the construction of a radio map based on interpolation from a sparsely deployed set of distributed sensors is a promising technique for monitoring spectrum usage. Two currently available weighted-sum methods, inverse distance weighting (IDW) and natural neighbor (NaN), have an important 'robustness' attribute in addition to not requiring knowledge of the spatial correlation function: They also do not require knowledge of the emitter location, or even knowledge of how many emitters are active; for each method, the operation is independent of this information. In the case of a single emitter of known location, the stochastic methods (SM) proposed here can estimate path loss parameters to gain an advantage, and the result has been shown to be lower RMS errors in estimating

radio power. Notably, the most practical approach, SM-2, has low error in comparison with NaN and IDW when D/Xc ranges between 0 and 1 where D is the inter-sensor spacing and X_c is the shadow-fading correlation distance. Also, using SM-2, RMS error is robust to the emitter location and other conditions. For the most part, however, either IDW or NaN can be used as backup interpolation methods whenever the single-emitter location, or number of emitters, is unknown. The opportunities suggested by this observation are worthy of further study.

In the last part, we investigated inter-system interference in shared spectrum scenarios by exploring the specific case of Wi-Fi and LTE coexistence in emerging unlicensed frequency bands. We developed an analytical model for the performance evaluation along with consideration of distinct MAC layer features of both the technologies. The interference model has been partially verified via experimental evaluations using USRP-based SDR platforms on the ORBIT testbed available at WINLAB. The results showed the significant performance degradation due to the uncoordinated operation of Wi-Fi and LTE in the shared band. To address this problem, we proposed optimization based logically centralized coordination algorithms across Wi-Fi and LTE systems - (1) power control at both Wi-Fi and LTE nodes which maximize aggregate throughput across all clients in the network considering throughput requirement at each link, and (2)a time division channel access which provides channel access to each RAT individually and brings fairness between networks of both RATs. We deduced that as the number of links grows, coordinated optimization results in allocation of orthogonal resources (e.g. separate channels) giving greater benefit than full sharing of the same spectrum space, as is the case for power control optimization. In future work, we plan to extend our analytical model and optimization framework to study realistic user applications for which full buffer traffic conditions cannot be assumed. We further plan to extend the optimization framework to exploit the frequency diversity for joint coordination of Wi-Fi and LTE.

References

[1] Samsung, "Vision and key features for 5th generation (5G) cellular," 2014, http://tinyurl.com/lo5gg53.

[2] S. Giri, "Exploring 5G: Performance targets, technologies and timelines," 2014, http://tinyurl.com/mznelg8.

[3] J. Kamran Etemad, LTE World Summit, "Improving cell capacity of 5G systems through opportunistic use of unlicensed and shared spectrum," 2014, http://tinyurl.com/k4bwjw4.

[4] A. T. Moray Rumney, "Taking 5G from vision to reality," 2014, the 6th Future of Wireless International Conference, http://tinyurl.com/o8hug8j.

[5] "Cisco Visual Networking Index: global mobile data traffic forecast update, 2013-2018," cisco White Paper, Feb 2014.

[6] M. , W. Lehr, A. Acker, and M. Gomez, "Socio-technical considerations for spectrum access system (sas) design," in *Dynamic Spectrum Access Networks (DySPAN), 2015 IEEE International Symposium on*, Sept 2015, pp. 35–46.

[7] P. C. of Advisors on Science and Technology, "Realizing the full potential of government-held spectrum to spur economic growth," [Online]. Available: http://www.whitehouse.gov/sites/default/files/microsites/ostp/pcast spectrum report final july 20 2012.pdf.

[8] S. Shellhammer, A. Sadek, and W. Zhang, "Technical challenges for cognitive radio in the TV white space spectrum," in *Information Theory and Applications Workshop, 2009*, Feb 2009, pp. 323–333.

[9] F. C. Commission, "Enabling innovative small cell use in 3.5 GHz band NPRM and order," fCC 12-148, 2012.

[10] RP-140060, "Summary of a workshop on LTE in unlicensed spectrum," 3GPP TSG-RAN Meeting 63, 2014.

[11] I. C. Ali Sadri, "mmWave technology evolution from WiGig to 5G small cells," 2013, http://tinyurl.com/lejlgfg.

[12] S. Sagari, I. Seskar, and D. Raychaudhuri, "Modeling the coexistence of LTE and WiFi heterogeneous networks in dense deployment scenarios," accepted at IEEE ICC workshop 2015 on LTE in Unlicensed Bands: Potentials and Challenges.

[13] B. Sadiq, R. Madan, and A. Sampath, "Downlink scheduling for multiclass traffic in lte," *EURASIP J. Wirel. Commun. Netw.*, vol. 2009, pp. 14:9–14:9, Mar. 2009. [Online]. Available: http://dx.doi.org/10.1155/2009/510617

[14] G. Bianchi, ""Performance analysis of the IEEE 802.11 distributed coordination function"," *IEEE Journal on Selected Areas in Communications*, vol. 18, no. 3, pp. 535 –547, 2000.

[15] A. Baid, M. Schapira, I. Seskar, J. Rexford, and D. Raychaudhuri, "Network cooperation for client-AP association optimization," in *IEEE WiOpt*, 2012, pp. 431 –436.

[16] M. Buddhikot, P. Kolodzy, S. Miller, K. Ryan, and J. Evans, "Dimsumnet: new directions in wireless networking using coordinated dynamic spectrum," in *World of Wireless Mobile and Multimedia Networks, 2005. WoWMoM 2005. Sixth IEEE International Symposium on a*, June 2005, pp. 78–85.

[17] V. Brik, E. Rozner, S. Banerjee, and P. Bahl, "Dsap: a protocol for coordinated spectrum access," in *New Frontiers in Dynamic Spectrum Access Networks, 2005. DySPAN 2005. 2005 First IEEE International Symposium on*, Nov 2005, pp. 611–614.

[18] O. Ileri, D. Samardzija, and N. Mandayam, "Demand responsive pricing and competitive spectrum allocation via a spectrum server," in *New Frontiers in Dynamic Spectrum Access Networks, 2005. DySPAN 2005. 2005 First IEEE International Symposium on*, Nov 2005, pp. 194–202.

[19] X. Jing and D. Raychaudhuri, ""Spectrum Co-existence of IEEE 802.11b and 802.16a Networks Using Reactive and Proactive Etiquette Policies"," *ACM Mob. Netw. Appl.*, pp. 539–554, 2006. [Online]. Available: http://dx.doi.org/10.1007/s11036-006-7321-z

[20] R. Murty, R. Chandra, T. Moscibroda, and P. Bahl, "Senseless: A database-driven white spaces network," *Mobile Computing, IEEE Transactions on*, vol. 11, no. 2, pp. 189–203, Feb 2012.

[21] Google, "Google spectrum database," link: https://www.google.com/get/spectrumdatabase/.

[22] S. Sagari, A. Baid, I. Seskar, T. Murase, M. Oguchi, and D. Raychaudhuri, "Performance evaluation of mobile hotspots in densely deployed WLAN environments"," in *IEEE PIMRC*, 2013.

[23] S. Sagari, L. Greenstein, and W. Trappe, "Emulating co-channel interference in wireless networks using equivalent low-tap filters," in *Information Sciences and Systems (CISS), 2014 48th Annual Conference on*, March 2014, pp. 1–6.

[24] S. Sagari, W. Trappe, and L. Greenstein, "Equivalent tapped delay line channel responses with reduced taps," in *Vehicular Technology Conference (VTC Fall), 2013 IEEE 78th*, Sept 2013, pp. 1–5.

[25] S. Sagari, S. Baysting, D. Saha, I. Seskar, W. Trappe, and D. Raychaudhuri, "Coordinated dynamic spectrum management of lte-u and wi-fi networks," in *Dynamic Spectrum Access Networks (DySPAN), 2015 IEEE International Symposium on*, Sept 2015, pp. 209–220.

[26] D. Raychaudhuri and A. Baid, "NASCOR: Network assisted spectrum coordination service for coexistence between heterogeneous radio systems," *IEICE Trans. Commun.*, vol. 97, no. 2, pp. 251–260, 2014. [Online]. Available: http://ci.nii.ac.jp/naid/130003394616/en/

[27] X. Jin, L. E. Li, L. Vanbever, and J. Rexford, "Softcell: Scalable and flexible cellular core network architecture," in *Proceedings of the Ninth ACM Conference on Emerging Networking Experiments and Technologies*, ser. CoNEXT '13. New York, NY, USA: ACM, 2013, pp. 163–174. [Online]. Available: http://doi.acm.org/10.1145/2535372.2535377

[28] ""T-Mobile 4G mobile hotspot"," http://www.t-mobile.com/shop/phones/cell-phone-detail.aspx?cell-phone=t-mobile-4g-mobile-hotspot.

[29] ""Verizon - mobile broadband"," http://tinyurl.com/knsk2s.

[30] H. Han, Y. Liu, G. Shen, Y. Zhang, and Q. Li, ""DozyAP: power-efficient Wi-Fi tethering"," in *Proceedings of ACM MobiSys*, 2012, pp. 421–434. [Online]. Available: http://doi.acm.org/10.1145/2307636.2307675

[31] ""Cisco Visual Networking Index: global mobile data traffic forecast update, 2011-2016"," cisco White Paper, Feb 2012.

[32] ""Most 2014 GM cars will also be a Wi-Fi hotspot"," http://www.nbcnews.com/business/most-2014-gm-cars-will-also-be-wi-fi-hotspot-1C8539395.

[33] ""Easy to Beat: Next-Gen cardiac care includes wireless pacemakers"," http://www.scientificamerican.com/article.cfm?id=wireless-cardiac-pacemaker.

[34] M. A. Ergin, K. Ramachandran, and M. Gruteser, ""Understanding the effect of access point density on wireless LAN performance"," in *Proceedings of ACM MobiCom*, 2007, pp. 350–353. [Online]. Available: http://doi.acm.org/10.1145/1287853.1287902

[35] J. Hare, L. Hartung, and S. Banerjee, ""Beyond deployments and testbeds: experiences with public usage on vehicular WiFi hotspots"," in *Proceedings of ACM MobiSys*, 2012, pp. 393–406. [Online]. Available: http://doi.acm.org/10.1145/2307636.2307673

[36] R. Ando, T. Murase, and M. Oguchi, ""Characteristics of Qos-guaranteed TCP on real mobile terminal in wireless LAN"," in *IEEE International Workshop Technical Committee on Communications Quality and Reliability (CQR)*, 2011, pp. 1–6.

[37] J. Huang, F. Qian, A. Gerber, Z. M. Mao, S. Sen, and O. Spatscheck, "A close examination of performance and power characteristics of 4G LTE networks," in *Proceedings of ACM MobiSys*, 2012, pp. 225–238. [Online]. Available: http://doi.acm.org/10.1145/2307636.2307658

[38] ""Capacity coverage and deployment considerations for IEEE 802.11g"," cisco White Paper, http://tinyurl.com/9hye7.

[39] D. Malone, K. Duffy, and D. Leith, ""Modeling the 802.11 distributed coordination function in nonsaturated heterogeneous conditions"," *IEEE/ACM Transactions on Networking*, vol. 15, no. 1, pp. 159–172, 2007. [Online]. Available: http://dx.doi.org/10.1109/TNET.2006.890136

[40] F. Daneshgaran, M. Laddomada, F. Mesiti, and M. Mondin, "Unsaturated throughput analysis of ieee 802.11 in presence of non ideal transmission channel and capture effects," *Wireless Communications, IEEE Transactions on*, vol. 7, no. 4, pp. 1276 –1286, april 2008.

[41] M. Achanta, ""Method and apparatus for least congested channel scan for wireless access points"," 2006, uS Patent No. 20060072602.

[42] "Ar9462: Single-chip, 2.4/5 ghz, 2-stream 802.11a/b/g/n and bt 4.0 + hs soc solution with sst technology," http://tinyurl.com/n9n2lfj.

[43] dBm, "Satellite Link Emulator," "http://www.dbmcorp.com/Code/SLE.asp".

[44] R. L. A. K. Company, "Channel Simulator (T400CS)," "http://tinyurl.com/c2d6s3f".

[45] C. Mehlfuhrer and M. Rupp, ""Approximation and resampling of tapped delay line channel models with guaranteed channel properties"," in *Acoustics, Speech and Signal Processing, 2008. ICASSP 2008. IEEE International Conference on*, 31 2008-april 4 2008, pp. 2869 –2872.

[46] K. Borries, G. Judd, D. Stancil, and P. Steenkiste, ""FPGA-based Channel Simulator for a Wireless Network Emulator"," in *Vehicular Technology Conference, 2009. VTC Spring 2009. IEEE 69th*, april 2009, pp. 1 –5.

[47] F. Ren and Y. Zheng, ""A low-complexity hardware implementation of discrete-time frequency-selective rayleigh fading channels"," in *Circuits and Systems, 2009. ISCAS 2009. IEEE International Symposium on*, may 2009, pp. 1759 –1762.

[48] M. Kahrs and C. Zimmer, ""Digital signal processing in a real-time propagation simulator"," *Instrumentation and Measurement, IEEE Transactions on*, vol. 55, no. 1, pp. 197 – 205, feb. 2006.

[49] P. Hoeher, ""A statistical discrete-time model for the WSSUS multipath channel"," *Vehicular Technology, IEEE Transactions on*, vol. 41, no. 4, pp. 461 –468, nov 1992.

[50] V. Tripathi, A. Mantravadi, and V. Veeravalli, ""Channel acquisition for wideband CDMA signals"," *Selected Areas in Communications, IEEE Journal on*, vol. 18, no. 8, pp. 1483 –1494, aug. 2000.

[51] A. F. Molisch, ""Wireless Communications"," wiley and Sons, 2nd ed., 2011; Scn. 7.3.2.

[52] D. Cox, "910 mhz urban mobile radio propagation: Multipath characteristics in new york city," *Vehicular Technology, IEEE Transactions on*, vol. 22, no. 4, pp. 104 – 110, nov 1973.

[53] D. Cassioli, M. Win, and A. Molisch, ""The ultra-wide bandwidth indoor channel: from statistical model to simulations"," *Selected Areas in Communications, IEEE Journal on*, vol. 20, no. 6, pp. 1247 – 1257, aug 2002.

[54] V. Erceg, D. Michelson, S. Ghassemzadeh, L. Greenstein, A. Rustako, P. Guerlain, M. Dennison, R. Roman, D. Barnickel, S. Wang, and R. Miller, ""A model for the multipath delay profile of fixed wireless channels"," *Selected Areas in Communications, IEEE Journal on*, vol. 17, no. 3, pp. 399–410, 1999.

[55] A. Goldsmith and S.-G. Chua, "Variable-rate variable-power mqam for fading channels," *Communications, IEEE Transactions on*, vol. 45, no. 10, pp. 1218 – 1230, oct 1997.

[56] R. D. Yates and D. J. Goodman, *Probability and stochastic processes.* Wiley, 1999.

[57] C. Phillips, D. Sicker, and D. Grunwald, "Bounding the error of path loss models," in *New Frontiers in Dynamic Spectrum Access Networks (DySPAN), 2011 IEEE Symposium on*, May 2011, pp. 71–82.

[58] M. Hata, "Empirical formula for propagation loss in land mobile radio services," *Vehicular Technology, IEEE Transactions on*, vol. 29, no. 3, pp. 317–325, Aug 1980.

[59] V. Erceg, L. Greenstein, S. Tjandra, S. Parkoff, A. Gupta, B. Kulic, A. Julius, and R. Bianchi, "An empirically based path loss model for wireless channels in suburban environments," *Selected Areas in Communications, IEEE Journal on*, vol. 17, no. 7, pp. 1205–1211, Jul 1999.

[60] C. Phillips, D. Sicker, and D. Grunwald, "A survey of wireless path loss prediction and coverage mapping methods," *Communications Surveys Tutorials, IEEE*, vol. 15, no. 1, pp. 255–270, First 2013.

[61] T. S. Rappaport, "Wireless communications: principles and practice," Ch. 3.9, Vol. 2, Prentice Hall PTR, 1996.

[62] A. Goldsmith, "Wireless communications," Ch. 2.6, Cambridge University Press, 2005.

[63] P. J. Bickel and K. A. Doksum, "Mathematical statistics : basic ideas and selected topics, volume I," Ch. 2, 2nd ed., Prentice Hall, 2001.

[64] J. A. Rice, "Mathematical statistics and data analysis," Ch. 8 and 14, 2nd ed., Duxbury Press, 1995.

[65] M. Gudmundson, "Correlation model for shadow fading in mobile radio systems," *Electronics Letters*, vol. 27, no. 23, pp. 2145–2146, Nov 1991.

[66] A. Goldsmith, L. Greenstein, and G. Foschini, "Error statistics of real-time power measurements in cellular channels with multipath and shadowing," *Vehicular Technology, IEEE Transactions on*, vol. 43, no. 3, pp. 439–446, Aug 1994.

[67] X. Zhao, L. Razouniov, and L. Greenstein, "Path loss estimation algorithms and results for rf sensor networks," in *Vehicular Technology Conference, 2004. VTC2004-Fall. 2004 IEEE 60th*, vol. 7, Sept 2004, pp. 4593–4596 Vol. 7.

[68] P. Agrawal and N. Patwari, "Correlated link shadow fading in multi-hop wireless networks," *Wireless Communications, IEEE Transactions on*, vol. 8, no. 8, pp. 4024–4036, August 2009.

[69] N. Cressie, "Statistics for spatial data," *Terra Nova*, vol. 4, no. 5, pp. 613–617, 1992. [Online]. Available: http://dx.doi.org/10.1111/j.1365-3121.1992.tb00605.x

[70] R. D. Yates and D. J. Goodman, *Probability and stochastic processes.* John Wiley and Sons, 1999.

[71] M. L. Eaton, *Multivariate Statistics: a Vector Space Approach.* John Wiley and Sons, 1983.

[72] M. Osborne, "Least squares and maximum likelihood."

[73] "3gpp tr 36.814 v9.0.0," *www.3gpp.org/ftp/Specs/archive/*36_*series*/36.814/.

[74] S. Ureten, A. Yongacoglu, and E. Petriu, "A comparison of interference cartography generation techniques in cognitive radio networks," in *Communications (ICC), 2012 IEEE International Conference on*, June 2012, pp. 1879–1883.

[75] P. Abrahamsen, *A Review of Gaussian Random Fields and Correlation Functions.* Norsk Regnesentral/Norwegian Computing Center, 1997. [Online]. Available: https://books.google.com/books?id=InByAAAACAAJ

[76] IEEE, "Part 11: Wireless LAN medium access control (MAC) and physical layer (PHY) specifications," 2012.

[77] K. Jamieson, B. Hull, A. Miu, and H. Balakrishnan, "Understanding the real-world performance of carrier sense," in *Proceedings of the 2005 ACM SIGCOMM Workshop on Experimental Approaches to Wireless Network Design and Analysis*, ser. E-WIND '05. New York, NY, USA: ACM, 2005, pp. 52–57. [Online]. Available: http://doi.acm.org/10.1145/1080148.1080160

[78] C. F. S., C. A. M., A. E. P. L., A. F. M. Jr., V. R. D., C. S., and D. K., "LTE/Wi-Fi coexistence: Challenges and mechanisms," 2013, xXXI SIMPOSIO BRASILEIRO DE TELECOMUNICACOES - SBrT2013.

[79] F. Abinader, E. Almeida, F. Chaves, A. Cavalcante, R. Vieira, R. Paiva, A. Sobrinho, S. Choudhury, E. Tuomaala, K. Doppler, and V. Sousa, "Enabling the coexistence of lte and wi-fi in unlicensed bands," *Communications Magazine, IEEE*, vol. 52, no. 11, pp. 54–61, Nov 2014.

[80] X. Jing and D. Raychaudhuri, "Spectrum co-existence of ieee 802.11b and 802.16a networks using reactive and proactive etiquette policies," *Mobile Networks and Applications*, vol. 11, no. 4, pp. 539–554, 2006. [Online]. Available: http://dx.doi.org/10.1007/s11036-006-7321-z

[81] A. Baid, S. Mathur, I. Seskar, S. Paul, A. Das, and D. Raychaudhuri, "Spectrum mri: Towards diagnosis of multi-radio interference in the unlicensed band," in *Wireless Communications and Networking Conference (WCNC), 2011 IEEE*, March 2011, pp. 534–539.

[82] G. Nychis, C. Tsourakakis, S. Seshan, and P. Steenkiste, "Centralized, measurement-based, spectrum management for environments with heterogeneous wireless networks," in *Dynamic Spectrum Access Networks (DYSPAN), 2014 IEEE International Symposium on*, April 2014, pp. 303–314.

[83] E. Almeida, A. Cavalcante, R. Paiva, F. Chaves, F. Abinader, R. Vieira, S. Choudhury, E. Tuomaala, and K. Doppler, "Enabling LTE/WiFi coexistence by LTE blank subframe allocation," in *2013 IEEE International Conference on Communications (ICC)*, June 2013, pp. 5083–5088.

[84] S. Baghel, M. Ingale, and G. Goyal, "Coexistence possibilities of lte with ism technologies and gnss," in *Communications (NCC), 2011 National Conference on*, Jan 2011, pp. 1–5.

[85] A. Cavalcante, E. Almeida, R. Vieira, F. Chaves, R. Paiva, F. Abinader, S. Choudhury, E. Tuomaala, and K. Doppler, "Performance evaluation of LTE and Wi-Fi coexistence in unlicensed bands," in *2013 IEEE 77th Vehicular Technology Conference (VTC Spring)*, June 2013, pp. 1–6.

[86] I. Qualcomm Technologies, "LTE in unlicensed spectrum: Harmonious coexistence with Wi-Fi," 2014, white paper.

[87] R. Ratasuk, M. Uusitalo, N. Mangalvedhe, A. Sorri, S. Iraji, C. Wijting, and A. Ghosh, "License-exempt LTE deployment in heterogeneous network," in *Wireless Communication Systems (ISWCS), 2012 International Symposium on*, Aug 2012, pp. 246–250.

[88] F. Liu, E. Bala, E. Erkip, and R. Yang, "A framework for femtocells to access both licensed and unlicensed bands," in *Modeling and Optimization in Mobile, Ad Hoc and Wireless Networks (WiOpt), 2011 International Symposium on*, May 2011, pp. 407–411.

[89] T. Nihtila, V. Tykhomyrov, O. Alanen, M. Uusitalo, A. Sorri, M. Moisio, S. Iraji, R. Ratasuk, and N. Mangalvedhe, "System performance of LTE and IEEE 802.11 coexisting on a shared frequency band," in *Wireless Communications and Networking Conference (WCNC), 2013 IEEE*, April 2013, pp. 1038–1043.

[90] F. Chaves, E. Almeida, R. Vieira, A. Cavalcante, F. Abinader, S. Choudhury, and K. Doppler, "LTE UL power control for the improvement of LTE/Wi-Fi coexistence," in *2013 IEEE 78th Vehicular Technology Conference (VTC Fall)*, Sept 2013, pp. 1–6.

[91] R. Paiva, P. Papadimitriou, and S. Choudhury, "A physical layer framework for interference analysis of LTE and Wi-Fi operating in the same band," in *2013 Asilomar Conference on Signals, Systems and Computers*, Nov 2013, pp. 1204–1209.

[92] D. Raychaudhuri, I. Seskar, M. Ott, S. Ganu, K. Ramachandran, H. Kremo, R. Siracusa, H. Liu, and M. Singh, "Overview of the orbit radio grid testbed for evaluation of next-generation wireless network protocols," in *Wireless Communications and Networking Conference, 2005 IEEE*, vol. 3, March 2005, pp. 1664–1669 Vol. 3.

[93] E. Research, "Usrp b200 and b210," http://tinyurl.com/k7w6zh2.

[94] L. W. ath9k, https://wireless.wiki.kernel.org/en/users/drivers/ath9k.

[95] "hostapd: Ieee 802.11 ap, ieee 802.1x/wpa/wpa2/eap/radius authenticator," http://w1.fi/hostapd/.

[96] N. Nikaein, M. K. Marina, S. Manickam, A. Dawson, R. Knopp, and C. Bonnet, "Openairinterface: A flexible platform for 5g research," *SIGCOMM Comput. Commun. Rev.*, vol. 44, no. 5, pp. 33–38, Oct. 2014. [Online]. Available: http://doi.acm.org/10.1145/2677046.2677053

[97] L. Wireless, https://wireless.wiki.kernel.org/en/users/documentation/iw.

[98] A. Gudipati, D. Perry, L. E. Li, and S. Katti, "Softran: Software defined radio access network," in *Proceedings of the Second ACM SIGCOMM Workshop on Hot Topics in Software Defined Networking*, ser. HotSDN '13. New York, NY, USA: ACM, 2013, pp. 25–30. [Online]. Available: http://doi.acm.org/10.1145/2491185.2491207

[99] M. Chiang, C. W. Tan, D. Palomar, D. O'Neill, and D. Julian, "Power control by geometric programming," *Wireless Communications, IEEE Transactions on*, vol. 6, no. 7, pp. 2640–2651, July 2007.